

Polarized multiwavelength emission from pulsar wind – accretion disk interaction in a transitional millisecond pulsar

M. C. Baglio^{*1}, F. Coti Zelati^{*2, 3, 1}, A. Di Marco⁴, F. La Monaca⁴, A. Papitto⁵, A. K. Hughes^{6, 7}, S. Campana¹, D. M. Russell⁸, D. F. Torres^{2, 3, 9}, F. Carotenuto^{5, 7}, S. Covino^{1, 10}, D. de Martino¹¹, S. Giarratana¹, S. E. Motta¹, K. Alabarta⁸, P. D’Avanzo¹, G. Illiano⁵, M. M. Messa^{1, 12}, A. Miraval Zanon¹³, and N. Rea^{2, 3}

¹INAF–Osservatorio Astronomico di Brera, Via Bianchi 46, I-23807 Merate (LC), Italy

²Institute of Space Sciences (ICE, CSIC), Campus UAB, Carrer de Can Magrans s/n, E-08193 Barcelona, Spain

³Institut d’Estudis Espacials de Catalunya (IEEC), 08860 Castelldefels (Barcelona), Spain

⁴INAF Istituto di Astrofisica e Planetologia Spaziali, Via del Fosso del Cavaliere 100, I-00133 Rome, Italy

⁵INAF–Osservatorio Astronomico di Roma, Via Frascati 33, I-00078 Monteporzio Catone (RM), Italy

⁶Department of Physics, University of Alberta, Edmonton, T6G 2E1, Canada

⁷Astrophysics, Department of Physics, University of Oxford, Keble Road, Oxford, OX1 3RH, UK

⁸Center for Astrophysics and Space Science, New York University Abu Dhabi, PO Box 129188, Abu Dhabi, UAE

⁹Institució Catalana de Recerca i Estudis Avançats (ICREA), Passeig Lluís Companys 23, E-08010 Barcelona, Spain

¹⁰Como Lake centre for AstroPhysics (CLAP), DiSAT, Università dell’Insubria, via Valleggio 11, 22100 Como, Italy

¹¹INAF–Osservatorio Astronomico di Capodimonte, Salita Moiariello 16, I-80131 Naples, Italy

¹²Dipartimento di Fisica, Università degli Studi di Milano, Via Celoria 16, I-20133, Milan, Italy

¹³ASI - Agenzia Spaziale Italiana, Via del Politecnico snc, I-00133 Rome, Italy

Abstract

Transitional millisecond pulsars (tMSPs) bridge the evolutionary gap between accreting neutron stars in low-mass X-ray binaries and millisecond radio pulsars. These systems exhibit a unique subluminescent X-ray state characterized by the presence of an accretion disk and rapid switches between high and low X-ray emission modes. The high mode features coherent millisecond pulsations spanning from the X-ray to the optical band. We present multiwavelength polarimetric observations of the tMSP PSR J1023+0038 aimed at conclusively identifying the physical mechanism powering its emission in the subluminescent X-ray state. During the high mode, we detect polarized emission in the 2–6 keV energy range, with a polarization degree of $(12 \pm 3)\%$ and a polarization angle of $-2^\circ \pm 9^\circ$ (1σ) measured counterclockwise from the North celestial pole towards East. At optical wavelengths, we find a polarization degree of $(1.41 \pm 0.04)\%$ and a polarization angle aligned with that in the soft X-rays, suggesting a common physical mechanism operating across these bands. Remarkably, the polarized flux spectrum matches the pulsed emission spectrum from optical to X-rays. The polarization properties differ markedly from those observed in other accreting neutron stars and isolated rotation-powered pulsars and are also inconsistent with an origin in a compact jet. Our results provide direct evidence that the polarized and pulsed emissions both originate from synchrotron radiation at the shock formed where the pulsar wind interacts with the inner regions of the accretion disk.

1 Introduction

The evolution of accreting neutron stars (NSs) in low-mass X-ray binaries (LMXBs) as progenitors

^{*} These authors contributed equally to this work.

of millisecond radio pulsars (MSPs) involves distinct phases [1], with transitional MSPs (tMSPs) representing one of the most intriguing stages of this process due to their unique properties [23, 95]. PSR J1023+0038 (hereafter J1023) is the prototypical tMSP [4], offering an exceptional opportunity to study these enigmatic objects in detail. Detected in 2007 as a radio MSP with a spin period of 1.69 ms, J1023 orbits a $0.24 M_{\odot}$ star every 4.75 hours [4]. In 2013, J1023 experienced dramatic changes in its emission properties, ceasing its radio pulsations and exhibiting increased emission across the electromagnetic spectrum [112, 101]. J1023 has since remained in an active state, characterized by subluminescent X-ray emission with an average luminosity of $\simeq 7 \times 10^{33} \text{ erg s}^{-1}$ in the 0.3–80 keV energy range [33] – over four orders of magnitude below the Eddington luminosity for a NS. This emission alternates between high-intensity (70–80% of the time) and low-intensity (20–30%) modes, with occasional brief flares reaching $\approx 10^{35} \text{ erg s}^{-1}$ [96, 81, 5, 18]. Mode switches occur within 10–30 s, with low modes lasting from tens of seconds to minutes. During the high mode, J1023 exhibits coherent pulsed emission at the pulsar spin period at X-ray, ultraviolet (UV), and optical wavelengths, pointing to processes linked to the NS rotation [5, 98, 90, 70]. This pulsed emission disappears during the low mode. The UV, optical, and near-infrared emissions mainly originate from an accretion disk surrounding the NS and the irradiated companion star, leading to flickering and flaring [74, 97, 59, 109]. Bright radio and mm continuum emission is observed, with increased radio emission during the low mode and brief mm-band flares during switches from high to low modes [37, 19, 10].

The unique behavior of J1023 raises fundamental questions about the mechanisms powering its emission in the active state. J1023 releases rotational kinetic energy at a rate of $\simeq 4.4 \times 10^{34} \text{ erg s}^{-1}$ [3], about six times its average X-ray luminosity. This has sparked debates on whether the emission of tMSPs like J1023 in this active state is powered by pulsar rotation, mass accretion, or a combination of both [19, 98, 122, 82]. Multiband polarization measurements provide a key diagnostic tool for investigating these processes and solving this enigma.

This paper presents the results from the first multiwavelength polarimetric campaign of J1023 and is structured as follows. Section 2 describes the observations and data processing techniques employed across the X-ray, optical, and radio bands using the *Imaging X-ray Polarimetry Explorer* (IXPE), the *Neutron Star Interior Composition Explorer Mission* (NICER), the *Neil Gehrels Swift Observatory* (*Swift*), the *Very Large Telescope* (VLT), and the *Karl G.*

Jansky Very Large Array (VLA). Section 3 details the data analysis and results, encompassing the selection of emission modes and timing analysis of the IXPE data, and the polarimetric analysis across different wavelengths. We also present the spectral energy distributions (SEDs) derived from our observations. Section 4 discusses the implications of our findings on the emission mechanisms powering J1023 during its active state, evaluating scenarios such as accretion-powered processes, rotation-powered mechanisms analogous to isolated pulsars, and interactions between the pulsar wind and the accretion flow. Section 5 summarizes how our multiwavelength polarimetric observations provide critical insights into the enigmatic behavior of tMSPs like J1023.

2 The multi-wavelength dataset

We acquired multiwavelength data of J1023 using space-borne and ground-based telescopes. This section describes the observations and the procedures used for data processing and analysis (for more details, see Appendix A). All timestamps are referenced to the Solar System barycenter using the JPL DE440 ephemeris and the position: RA = $10^{\text{h}}23^{\text{m}}47^{\text{s}}.69$, Dec = $+00^{\circ}38'40.''8$ (J2000.0; [36]).

2.1 IXPE Observations

IXPE observed J1023 during two sessions: May 29–June 2 and June 3–June 14, 2024 (MJD 60459.52–60463.76; MJD 60464.88–60475.62). The total exposure time per detector unit (DU) was $\simeq 675$ ks. To reduce instrumental background, we applied the rejection algorithm by [40]¹. Source photons were extracted from a circle of $60''$ radius centered on the source, and background photons from an annulus with radii of $150''$ and $300''$. Emission modes were selected as detailed in Appendix B. Due to background dominance above 6 keV, we restricted the polarimetric analysis to the 2–6 keV band. Data processing was performed using the *ixpeobssim* package [11]. Spectral and spectro-polarimetric analyses were conducted with *HEASoft* and *FTOOLS* using the latest calibration files.

2.2 NICER Observations

During the IXPE campaign, we conducted two NICER observations of J1023 (Table 2) to guide the selection of high and low-mode episodes in the IXPE dataset. These observations were performed during orbit night-time to avoid optical light leak due

¹<https://github.com/aledimarco/IXPE-background>

to a damaged thermal shield². We reprocessed the data using NICERDAS version 13 in HEASoft and calibration products from 2024 February 6. We calibrated and screened the data using `nicer12`, and extracted 0.5–10 keV time series binned at 10 s using `nicer13-1c`. The background level was estimated with the SCORPEON model³.

2.3 *Swift* Observations

We performed two observations with *Swift* simultaneously with the VLA and VLT on 2024 June 4–5 (Table 2), using the X-ray Telescope (XRT) in photon counting mode and the Ultra-Violet/Optical Telescope (UVOT) in event mode with the UVM2 filter (central wavelength 226 nm; FWHM 52.7 nm). Data were processed using calibration files from 2024 May 22 for XRT and 2024 February 1 for UVOT. For XRT, we extracted source photons using a circular aperture of 47.2'' radius and background using an annulus with radii 94.4'' and 188.8''. We extracted background-subtracted 0.5–10 keV time series binned at 50 s (Fig. 9). For UVOT, we used `coordinator` and `uvotscreen` to obtain cleaned event lists, and extracted time series binned at 30 s using `uvotevt1c` (Fig. 9).

2.4 VLT Observations

We observed J1023 with the FOcal Reducer/low dispersion Spectrograph 2 (FORs2) on the VLT in polarimetric mode (Table 2). The observations were performed from 2024 June 4 at 23:34:37 UTC to 2024 June 5 at 00:39:23 UTC, under photometric conditions (seeing $\simeq 0.3''$). A total of 56 images were acquired using the $R_{\text{SPECIAL}+76}$ filter (R band; central wavelength 655 nm; FWHM 165 nm), each with a 20 s exposure, totaling 3946 s. A Wollaston prism and rotating half-wave plate (HWP) allowed images at four angles $\Phi_i = 22.5^\circ(i - 1)$, $i = 1, 2, 3, 4$. Four sets of images were acquired for each angle, repeated 14 times.

The images were bias-subtracted and flat-fielded. Aperture photometry was performed using the `daophot` tool [114] with a 6-pixel aperture. Using Equations 1–2 of [9], we calculated the normalized Stokes parameters Q_{opt} and U_{opt} . To estimate the degree and angle of linear polarization, we evaluated the parameter $S(\Phi)$ for each of the HWP angles, following [41] and references therein (see also [34, 9, 10]). This is linked to the polarization degree P_{opt} and

the angle θ by the formula:

$$S(\Phi) = P_{\text{opt}} \cos(2(\theta - \Phi)) \quad (1)$$

The parameters P_{opt} and θ were determined by maximizing the Gaussian likelihood function to provide an initial estimate for P_{opt} and θ and refining the estimates using a Markov Chain Monte Carlo (MCMC) procedure [67] (for further details on the algorithm, see [9, 10]). The polarization angle was calibrated using observations of the polarized standard star Vela 1-95, resulting in a correction of $1.6^\circ \pm 0.7^\circ$.

2.5 VLA Observations

We obtained simultaneous VLA radio observations of J1023 with *IXPE* and VLT from 2024 June 4 at 23:00:00 UTC to June 5 at 02:59:20 UTC. The source underwent a bright multi-wavelength flare starting at $\simeq 00:36:00$ UTC on June 5. We include here only the pre-flare data, yielding about 1.2 hr on-source.

We observed in C-band (central frequency $\simeq 6$ GHz) with a 3-bit sampler, dividing the 4096 MHz band into 32 spectral windows with 64 2-MHz channels each. Calibration used 3C286 (flux, bandpass), J1024–0052 (gain), and J1407+2827 (leakage). J1023 was monitored in $\simeq 9$ -min target scans bracketed by two 1-min secondary scans.

Data were processed using the CASA VLA pipeline [26], followed by manual and automated (`rflag` and `tfcrop`) radio frequency interference flagging. Cross-hand calibration followed standard VLA polarization procedures⁴; Stokes $IQUV$ images were created with `WSClean` [94]. After initial shallow deconvolution of the 10' field of view (FOV), we created a deconvolution mask using the unmasked Stokes I image, then iteratively refined imaging and performed phase-only self-calibration using `QuartiCal` [75]. We then subtracted background sources, allowing for narrow FOV images minimally affected by aliasing.

J1023 showed an average flux density of $\simeq 240 \mu\text{Jy}$ and experienced a short (~ 8 min) mini-flare peaking at $\simeq 500 \mu\text{Jy}$. We produced time-resolved $IQUV$ images in 1-min intervals and also created four deeper polarization images by combining multiple scans to boost signal-to-noise ratio at intervals corresponding to the times before the mini-flare, the mini-flare, the times after the mini-flare, and the combined times before and after the mini-flare. For each interval, `WSClean` generated 16 channelized images and a single frequency-averaged Multi-Frequency Synthesis (MFS) image. Flux densities were measured using

²https://heasarc.gsfc.nasa.gov/docs/nicer/analysis_threads/light-leak-overview/

³https://heasarc.gsfc.nasa.gov/docs/nicer/analysis_threads/scorpeon-overview/

⁴https://casaguides.nrao.edu/index.php/CASA_Guides:Polarization_Calibration_based_on_CASA_pipeline_standard_reduction:_The_radio_galaxy_3C75-CASA6.5.4

`imfit` in `CASA`, modeling the source as a point source with a synthesized beam-shaped Gaussian fit. 1σ uncertainties were derived from RMS noise estimates in nearby source-free regions using `imstat`, employing a circular aperture encompassing $\simeq \times 100$ synthesized beam areas. When signal-to-noise permitted, we fitted a power-law of the form $F_\nu \propto \nu^\alpha$ to channelized flux densities to determine the spectral index α .

3 Data Analysis and Results

Figure 1 shows the multiwavelength time series extracted from our dataset, along with the evolution of the optical and radio polarization properties. During the observations, we detected a single episode of low mode at X-ray and UV wavelengths lasting ≈ 5 min, matching an enhanced flux at both optical and radio wavelengths. In the following sections, we describe the multiwavelength timing and polarimetric properties of J1023 and present the SEDs of the total, pulsed, and polarized emissions.

3.1 Timing Analysis of the *IXPE* Dataset

Details on our timing analysis of X-ray data are provided in Appendix C. Coherent X-ray pulsations at the NS spin period in J1023 are detected only during the high mode [5, 71, 98, 70]. Hence, we used source photons collected by *IXPE* in the high mode in the 2–6 keV band for our analysis. We corrected photon arrival times for the pulsar’s orbital motion, using an orbital period of $P_{\text{orb}} = 17115.5216592$ s and a projected semi-major axis of $asini/c = 0.343356$ light-seconds [3]. We performed an epoch folding search around the expected spin frequency, sampling each spin cycle in 16 phase bins. We used a grid of T_{asc} values centered on the predicted value from [70], $T_{\text{asc}}^{\text{pred}} = 60461.97948(6)$ MJD. We recovered the coherent signal with an epoch folding variance of $S = 103$ (single-trial false alarm rate $p = 3.5 \times 10^{-15}$) at a spin frequency $\nu = 592.42146705(9)$ Hz and $T_{\text{asc}} = 60461.979580(14)$ MJD. The uncertainties were evaluated following [80] and from the Gaussian fit to the pulse variance distribution. The timing parameters are reported in Table 3⁵. Our measurement tends to favor a scenario where the pulsar’s rotational evolution in the subluminescent X-ray state remains largely unchanged compared to its behavior during the radio pulsar state (Fig. 11).

3.2 X-ray Polarimetric Properties

Details on the polarimetric analysis of the *IXPE* data are given in Appendix D. Within the 3–6 keV band,

Table 1: Polarization degree (P_X), angle (PA_X), and fit statistics (χ^2 , dof) measured in distinct X-ray energy bands by combining data from the three *IXPE* DUs using spectro-polarimetric analysis. Uncertainties are quoted at the 68.27% c.l.

Energy band (keV)	Average emission			High mode		
	P_X (%)	PA_X ($^\circ$)	$\chi^2(\text{dof})$	$P_{X,H}$ (%)	$PA_{X,H}$ ($^\circ$)	$\chi^2(\text{dof})$
2-6	11 ± 3	-7 ± 8	175(166)	12 ± 3	-2 ± 9	164(166)
2-3	8 ± 5	20 ± 20	32(31)	8 ± 6	10 ± 20	25(31)
3-6	15 ± 4	-9 ± 8	120(121)	15 ± 5	-3 ± 9	120(121)

we detected a polarization degree of $P_X = (16 \pm 5)\%$ and a polarization angle $PA_X = -7^\circ \pm 9^\circ$, measured counter-clockwise from the North celestial pole toward the East. This polarization degree exceeds the Minimum Detectable Polarization (MDP; [126, 45]) of 15% at 99% confidence, allowing us to reject the null hypothesis of unpolarized emission with 99.4% confidence (3.2σ significance; ⁶). In the 2–3 keV band, the polarization degree is consistent with zero within a 1σ uncertainty (see Fig. 2). By applying the same analysis to high-mode data, we obtain values consistent with the above (see Fig. 3), though none exceeded the MDP at 99% confidence. No variations in Stokes parameters were observed across the pulsar rotational cycle or the binary orbital cycle (for details, see Appendix D.3). For low-mode and flaring-mode data, the significance was too low for a reliable analysis, yielding upper limits of $P_{X,L} < 26\%$ and $P_{X,F} < 28\%$ at 90% confidence over the 2–6 keV range (Appendix D.1).

To improve the polarimetric measurements, we performed weighted spectro-polarimetric analyses [116, 38] on both the entire dataset and the high-mode dataset (Appendix D.2). We fitted a power-law model corrected for interstellar absorption [18, 33] and convolved with a constant polarization model to the data in the 2–6, 2–3 and 3–6 keV ranges. Results are summarized in Table 1. For the average emission in the 2–6 keV range, we obtained $P_X = (11 \pm 3)\%$ at $PA_X = -7^\circ \pm 8^\circ$. For the high-mode emission in the same range, we measured $P_{X,H} = (12 \pm 3)\%$ at $PA_{X,H} = -2^\circ \pm 9^\circ$. Figure 4 shows the confidence contours for the measurements of $P_{X,H}$ and $PA_{X,H}$ in the high mode across energy bands.

Previous analyses show that $\simeq 10\%$ of low-mode episodes in the *IXPE* datasets may be missed due to their short durations [5, 18, 33]. However, this does not affect the polarization degree measured during the high mode, as the potential increase, about 0.2% in the polarization degree, is within the measurement uncertainties (Appendix D.2).

⁵The timing model is archived at Zenodo.

⁶<https://heasarc.gsfc.nasa.gov/docs/ixpe/analysis/IXPEStats-Advice.pdf>

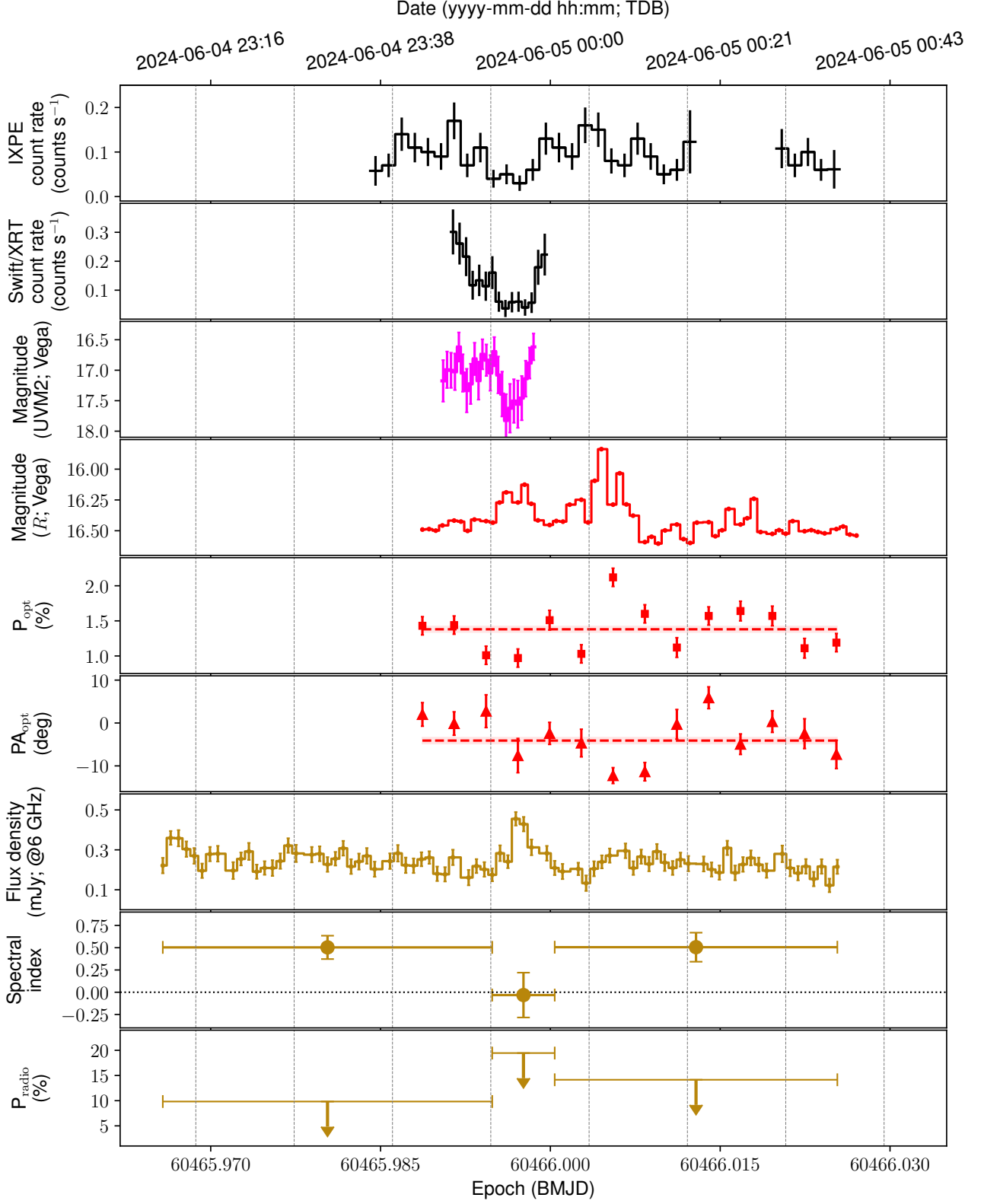


Figure 1: Multiwavelength time series and evolution of optical and radio polarization properties from *IXPE*, *Swift*, VLT, and VLA collected on 2024 June 4–5. Error bars represent 1σ c.l. (uncertainties in the fourth panel are smaller than markers). In panels five and six, red horizontal lines show the average optical polarization degree (P_{opt}) and angle (PA_{opt}), with shaded areas indicating $\pm 1\sigma$. In the eighth panel, the dotted line marks a flat spectrum. In the ninth panel, downward arrows indicate 3σ upper limits on the radio polarization fraction (P_{radio}).

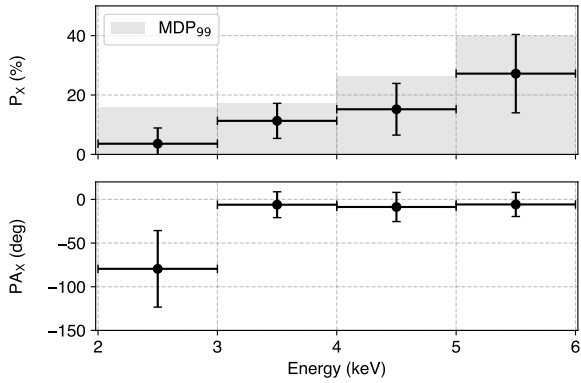
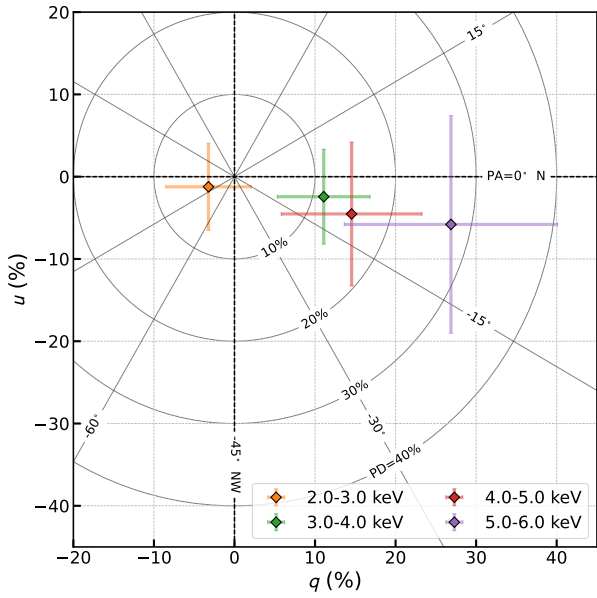


Figure 2: Top: normalized and background-subtracted Stokes parameters q and u for the average X-ray emission. The results are derived from an unbinned analysis of the combined data from all three DUs. The Stokes parameters were grouped into four bins with sizes of 1 keV across the 2–6 keV energy band. Each diamond represents the mean value, with error bars indicating the 1σ standard deviation. The circles give the contours of constant polarization degree while the radial lines correspond to constant polarization angle. Bottom: Energy dependence of the X-ray polarization in J1023. The top and bottom panels show the PD and PA as a function of photon energy estimated for the average X-ray emission using the formalism of [76]. The vertical error bars correspond to 1σ , while the horizontal bars reflect the width of the energy bins used for the binned analysis. Gray shaded areas show the minimum detectable polarization at the 99% c.l. for each bin.

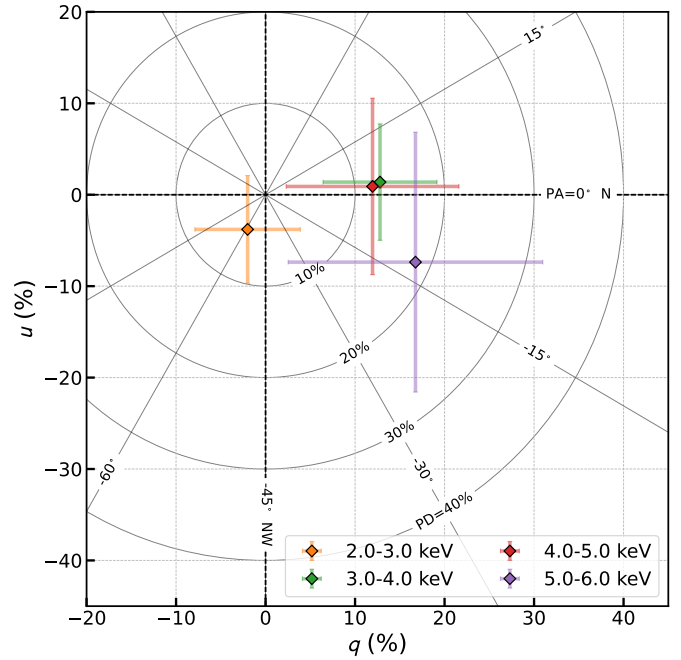


Figure 3: Same as in the top panel of Fig. 2, but for the X-ray emission in the high mode.

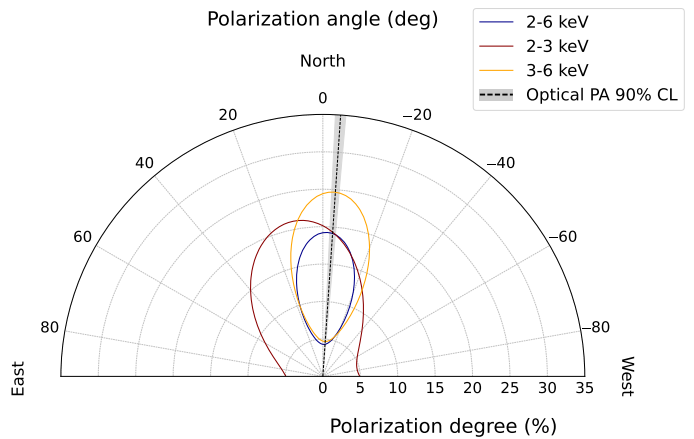


Figure 4: Protractor plot of X-ray polarization degree and angle for the high mode, compared with the optical polarization angle. The polarization degree and angle are measured over the energy ranges 2–6, 2–3, and 3–6 keV, and are displayed along the radial and azimuthal directions, respectively. Contours represent 90% confidence regions. The black dashed line and gray shaded area indicate the optical R -band polarization angle and its 90% c.l. uncertainty.

3.3 Optical Properties

Details on the optical properties of J1023 are presented in Appendix E. J1023 was detected at an average magnitude of $\simeq 16.4$ (Vega) in the R -band. We measured an average linear polarization degree of $P_{\text{opt}} = (1.38 \pm 0.04)\%$ and a polarization angle of $PA_{\text{opt}} = -4.1^\circ \pm 0.7^\circ$. During the X-ray high mode, we measured $P_{\text{opt,H}} = (1.41 \pm 0.04)\%$ at an angle $PA_{\text{opt,H}} = -3.9^\circ \pm 0.7^\circ$. This polarization angle is fully consistent with that derived at soft X-rays energies within the uncertainties (Fig. 4). In the X-ray low mode, we measured $P_{\text{opt,L}} = (0.97 \pm 0.13)\%$ and $PA_{\text{opt,L}} = -7.6^\circ \pm 4.0^\circ$, indicating a slight decrease in polarization degree during the low mode.

3.4 Radio Properties

J1023 exhibited an average flux density of $\simeq 240 \mu\text{Jy}$ at 6 GHz and experienced a mini-flare matching a low-mode episode in X-rays lasting $\simeq 8$ min, reaching a peak flux density of $\simeq 500 \mu\text{Jy}$. The power-law spectral index α remains nearly constant during the high-mode episodes that precede (H1) and follow (H2) the low mode, but decreases during the low mode (L): we obtain $\alpha_{\text{H1}} = 0.50 \pm 0.13$, $\alpha_{\text{H2}} = 0.51 \pm 0.16$ and $\alpha_{\text{L}} = -0.03 \pm 0.25$. Although the differences between modes do not exceed the 2σ significance threshold, the consistency of this trend with previous observations [19] points to optically thick synchrotron emission in the high mode and a mix of optically thick and optically thin synchrotron emission in the low mode.

These observations also provide the first constraints on the linear polarization fraction (P_{radio}) of the radio emission in both modes (Appendix A.5). We establish 3σ upper limits of $P_{\text{radio,H1}} < 10\%$, $P_{\text{radio,H2}} < 14\%$ and $P_{\text{radio,L}} < 19\%$. By stacking high-mode data, we achieved $P_{\text{radio,H}} < 9\%$.

3.5 Spectral Energy Distributions

To extract the SEDs shown in Fig. 5, we combined the fluxes for the emission in the high mode measured from *IXPE* and the VLT. Specifically, for the total SED we used the unabsorbed X-ray fluxes in the 2–3, 3–4 and 4–6 keV energy bands. For the optical data, we averaged the R -band fluxes from our VLT/FORS2 dataset during high modes. Adopting the estimated hydrogen column density ($N_{\text{H}} = 2.8 \times 10^{20} \text{ cm}^{-2}$), we calculated the V -band absorption coefficient based on the relation from [50] and determined the R -band absorption using the extinction laws from [58] (see also [57, 49, 55, 35]).

For the polarized SED, for the X-ray band we focused on the 2–3 keV and 3–6 keV energy ranges, using the polarization degrees measured during the

high mode through spectro-polarimetric analyses (see Table 1). The dereddened polarized optical flux was estimated by rescaling according to the polarization degree measured in the high mode, $(1.41 \pm 0.04)\%$.

For comparison, we overlaid the total and pulsed X-ray and optical fluxes obtained from a previous campaign involving the *XMM-Newton* and *NuSTAR* satellites as well as the SiFAP2 photometer mounted on the INAF *Telescopio Nazionale Galileo* [98]. Additionally, we included the fit of their SED of the pulsed emission using a single power law defined by $F_\nu = a \cdot \nu^b$, where F_ν is the flux density at frequency ν , a is the normalization constant, and b is the spectral index. Using nonlinear least squares fitting, the best-fit parameters were determined to be $a = (2.86 \pm 0.01) \times 10^{-13} \text{ erg cm}^{-2} \text{ s}^{-1}$, and $b = 0.288 \pm 0.015$ [98].

Our analysis shows that the SED of the polarized flux is consistent with the same power-law model that describes the spectrum of the pulsed signal. This provides additional strong evidence that the observed multiwavelength polarized emission shares a common origin with the pulsed emission across both optical and X-ray bands. Moreover, the near-coincidence of the polarized and pulsed fluxes throughout the spectrum indicates that the observed polarization originates almost entirely from the same emission processes responsible for the pulsations across the optical and X-ray frequencies. Theoretical predictions for the linear polarization of synchrotron radiation, assuming a spectral index $\alpha \simeq 1.7$ (as measured by [98] and shown in Fig. 5), suggest a theoretical maximum polarization degree of $\simeq 77\%$ [107], which is consistent with our findings. Future instrumentation designed to measure the polarization of pulsed emission will be essential to test this.

4 Discussion

4.1 The Nature of the Polarized Emission

4.1.1 An Accretion-powered Mechanism?

Our observations reveal that J1023 exhibits a higher soft X-ray polarization degree than any other accreting NSs in LMXBs with X-ray luminosities at least three orders of magnitude greater. In those systems, polarized X-ray emission is detected with polarization degrees of only a few percent and is primarily attributed to Comptonization, where seed photons from one or several regions near the NS scatter off high-energy particles ([119]; Appendix G). These regions are usually identified as areas on the NS surface where accreted material spreads due to rotational motion, transition zones where accreted material moves from the disk to the NS surface, or ex-

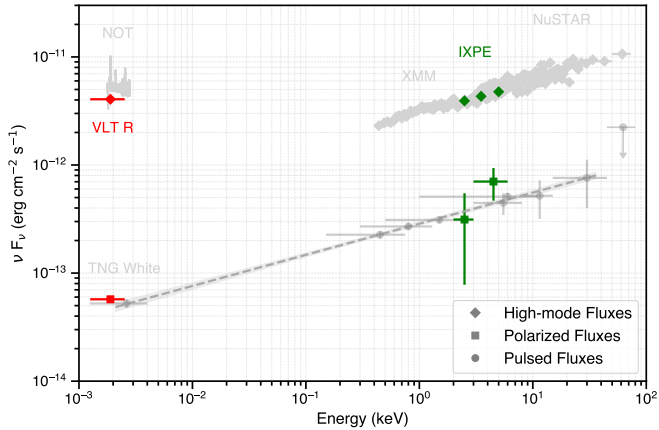


Figure 5: SEDs for the high mode of J1023 derived from *IXPE* and VLT high-mode fluxes (green and red diamonds), with polarized fluxes depicted as squares. High-mode fluxes and pulsed fluxes in the X-ray and optical bands derived by [98] are shown as light-gray diamonds and circles, respectively. The gray dashed line represents the power-law fit to the pulsed fluxes.

tended, geometrically thin plasma regions partially covering the disk. In some cases, additional polarized emission has been attributed to photons reflecting off the disk surface. Recently, X-ray radiation with a polarization degree of a few percent was detected from an accreting MSP during a bright outburst and attributed to moderately fan-beamed emission originating from small, heated spots on the NS surface [99]. The spectral properties of accreting NSs in LMXBs in spectral states similar to J1023 remain largely consistent across a wide range of X-ray luminosities, including levels comparable to those of J1023 [129, 83]. Hence, if similar emission mechanisms were at play in J1023, we would expect a polarization degree of a few percent at most. Our measured polarization degree exceeds this expectation, suggesting that these mechanisms are unlikely to be solely responsible for the observed polarization in J1023. This conclusion is further supported by theoretical considerations. Recent studies have demonstrated that emission from the spreading layer is expected to have a polarization degree not exceeding 1.5% [14] (see also [47]). Similarly, thermal Comptonization in accretion shocks above the surface of accreting MSPs results in a polarization degree of only a few percent at most [16].

4.1.2 Scattering in an Accretion Disk Wind?

Scattering of emission by outflows of highly ionized material launched from the accretion disk along the equatorial plane – commonly referred to as disk winds (e.g. [42]) – may provide an alternative source of polarization. Although there is currently no obser-

vational evidence for disk winds in J1023, recent work [93] suggests that even if such winds existed and significantly contributed to the X-ray emission from J1023, this mechanism alone cannot readily account for the high polarization degree at its known orbital inclination ($i = 46.4^{+0.5}_{-0.7}$; [115]). This conclusion holds true regardless of the wind opening angle, optical depth through the wind, or the nature and angular distribution of the illuminating X-ray emission, including scenarios with isotropic unpolarized sources, thermal radiation from the disk, or Comptonization [93].

4.1.3 A Rotation-powered Mechanism?

A few models have been developed to explain the X-ray to optical polarization properties in isolated pulsars, including the outer gap and two-pole caustic models, as well as current sheet models (for a review, see [60]). Assuming that the polarized emission from J1023 originates from mechanisms similar to those in isolated rotation-powered pulsars, we can then compare the polarization properties predicted by these models with those observed in J1023.

The outer gap (OG; [30, 31, 61, 117]) and two-pole caustic (TPC; [44]) models propose that the high-energy emission of pulsars originates from the outer magnetosphere, along the last open magnetic field lines inside the light cylinder radius. The emission mechanisms involve synchrotron radiation and curvature radiation from particles accelerated within vacuum gaps or extended regions of strong electric fields. Pulse profiles are characterized by caustics formed due to relativistic effects like aberration and light travel time delays. This results in double-peaked light curves, with peak separation depending on the magnetic inclination angle and the observer’s viewing angle. These models predict polarization properties such as rapid swings in the PA correlated with the pulses and dips in PD at the pulse peaks. The dips are attributed to depolarization from overlapping emissions originating from regions with varying magnetic field orientations. In the TPC model, rapid PA swings are expected through both peaks of the pulse profile. In contrast, the OG model predicts a significant PA swing mainly at the second peak, and the first peak may not show a strong PA swing unless the emission occurs near the light cylinder [43].

The PA in J1023 remains relatively constant across the pulse profile, at odds with the rapid PA swings predicted by the TPC model and, to some extent, the OG model. The PD remains relatively stable across the phase without significant dips at the pulse peaks, inconsistent with the expected PD dips due to depolarization from overlapping emissions.

Current sheet models [104, 28] focus on emission

from particles accelerated in the equatorial current sheet beyond the light cylinder. Magnetic reconnection in the current sheet accelerates particles, leading to high-energy synchrotron emission. Pulses are formed when the observer’s line of sight crosses the current sheet, resulting in one or two pulses per rotation. These models predict PD values typically $\simeq 15\text{--}30\%$, with PD dips at the pulse peaks due to depolarization effects. Significant PA swings are expected at the pulse peaks due to the reversal of the magnetic field polarity across the current sheet.

J1023 does not exhibit the sharp PA swings predicted by current sheet models or dips in the PD at the pulse peaks. The data suggest the emission region has a more uniform magnetic field orientation, inconsistent with the magnetic field reversals expected in current sheet models.

Overall, these discrepancies indicate that the emission mechanisms in J1023 differ from those assumed in standard models for isolated pulsars.

4.1.4 Pulsar Wind – Accretion Flow Interaction?

A scenario for the high mode of J1023 suggests the presence of an active rotation-powered pulsar, an accretion disk, and a compact jet. In this scenario, the observed X-ray, UV, and optical pulses originate from synchrotron emission at the surface of a shock region formed where the pulsar particle wind – modulated at the NS spin period – collides with the inner accretion flow [98, 122]. This interaction is thought to occur just beyond the light cylinder radius (the distance at which corotation with the pulsar becomes physically impossible), which is $\simeq 80$ km for J1023. The observed lag of $\simeq 150 \mu\text{s}$ between optical and X-ray pulses is suggested to originate from differences in the cooling timescales of synchrotron photons at these energies, given the expected magnetic field strength at the shock [98, 70]. A compact jet is launched, emitting partially self-absorbed synchrotron radiation from radio to infrared frequencies. Previous work shows that the shock emission contributes $\simeq 5\%$ of the optical flux and $\simeq 90\%$ of the soft X-ray flux, while the compact jet emission accounts for $\simeq 2.5\%$ in the optical band and $\simeq 10\%$ in soft X-rays [10].

Electrons spiraling along toroidal magnetic field lines around the jet axis emit synchrotron radiation, with the polarization oriented perpendicular to the field lines. Given this magnetic field geometry and the orbital inclination of J1023, calculations indicate that the expected polarization degree should not exceed $\simeq 25\%$ [123, 87, 77]. In the R -band, this translates to a maximum polarization degree of $\simeq 0.6\%$, which is lower than the average optical polariza-

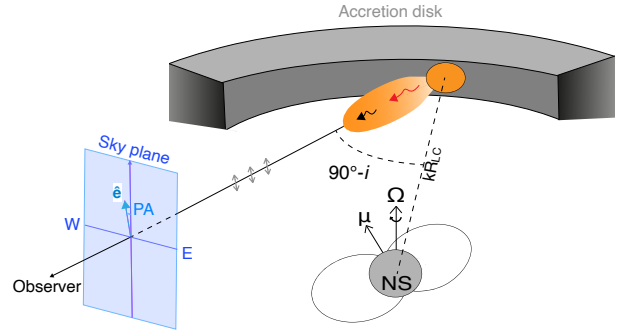


Figure 6: Geometry of polarized emission in the high mode of J1023. Pulsed emission originates from synchrotron emission at the shock surface where the pulsar particle wind – modulated at the NS rotational period – collides with the inner accretion flow at a distance of kR_{LC} ($k \simeq 1\text{--}2$; R_{LC} is the light cylinder radius; [98, 122]). Particles at the region visible to the observer (orange filled circle) emit synchrotron radiation boosted perpendicular to the shock surface (orange shaded area). Black and red wave-like arrows represent X-ray and optical photons emitted from the shock region. The average polarization angle (PA) is defined as the angle between the North-South direction on the sky plane (cyan parallelogram) and the projected electric field vector (\hat{e}). gray double-ended arrows represent the amplitude of the electric field (not to scale). μ and Ω denote the pulsar magnetic moment and angular velocity vector, respectively.

tion observed for J1023. In the $IXPE$ energy band, the limit is $\simeq 3\%$, again below our measured value. Hence, based on these considerations, we rule out the compact jet as the main source of the observed polarization.

If the observed low-level optical polarization is due to synchrotron radiation from the shock region, and a single population of electrons accelerated at the shock front produces synchrotron radiation from optical to X-rays, we would expect the intrinsic polarization in the optical band to propagate to higher energies. In this scenario, we estimate an intrinsic polarization degree of $12\text{--}17\%$ in the soft X-ray band [10]. Moreover, if the same region produces both optical and X-ray synchrotron radiation, their average polarization angles should align closely [10]. Our measurements are fully consistent with these predictions, providing striking evidence that the polarized emission in J1023 is driven by shock emission.

Figure 5 shows the SEDs of the high-mode flux, polarized flux, and pulsed flux of J1023 across optical and X-ray wavelengths. The SED of the polarized flux follows the same power law that describes the SED of the pulsed flux. Moreover, both the polarized and pulsed fluxes are consistent with each other.

These results indicate that the polarized and pulsed emissions share a common origin, providing strong support for the scenario in which the synchrotron-emitting shock region is the primary source of both in J1023.

Figure 6 illustrates the geometry of the system during the high mode. The pulsar wind, structured in toroidal segments with alternating magnetic field polarities, collides with the accretion flow, imprinting its magnetic field pattern onto the shock surface. Particles accelerated in the region of the shock visible to the observer gyrate along these field lines, emitting synchrotron radiation predominantly in the direction perpendicular to the shock surface. In this configuration, the electric field vector of the emitted radiation oscillates along the plane of the shock surface. The observed average PA of the X-ray and optical photons – defined as the angle between the North-South direction on the sky plane (perpendicular to the line of sight towards the observer) and the orientation of the electric field vector projected onto the sky plane – is determined by the geometry of the shock region as it appears from the observer’s viewpoint. The measured PA consistent with 0° indicates that, on average, the electric field vectors of the emitted X-ray and optical photons align with the North-South axis on the plane of the sky. The toroidal symmetry of the magnetic field and the positioning of the emission region in the pulsar equatorial plane ensure that the projected direction of the electric field vector – and thus the polarization angle – remains constant from the observer’s viewpoint, regardless of the pulsar rotational phase.

In the scenario outlined above, the upper limit on the radio linear polarization fraction in the high mode is consistent with partially self-absorbed synchrotron radiation from the optically thick portion of the compact jet (for more details on this result and on the polarization measurements in the low mode, see Appendix F).

4.2 Synchrotron Emission across Scales

Our findings reveal striking similarities between J1023 and pulsar wind nebulae (PWNe) regarding emission mechanisms and magnetic field geometry. In PWNe, the high-energy emission is attributed to synchrotron radiation produced by electrons accelerated within highly ordered, predominantly toroidal magnetic fields. These fields are shaped by the pulsar wind as it wraps around the pulsar and is compressed within the nebula (see, e.g., [105]). However, the polarization degree observed in a few PWNe is higher than in J1023. For instance, the Vela PWN exhibits an average soft X-ray polarization degree of $\approx 45\%$, with inner regions reaching up to 70% [131]. Ad-

ditionally, a polarization degree exceeding 60% has been detected in the outskirts (with 90% confidence; [84]). Similarly, the Crab PWN shows a spatially integrated PD of $\approx 20\%$ [20], with some regions exhibiting polarization degrees between 45% and 50% [84, 20]. The PWN around the pulsar PSR B0540–69 reaches a PD of $\simeq 25\%$ [132].

The distinct geometries and scales of PWNe compared to J1023 may play a crucial role in the observed differences. In PWNe, the pulsar wind expands into the surrounding environment over large distances, with the wind termination shock occurring at ≈ 0.1 pc from the pulsar [64, 103]. This extended region facilitates the development of large-scale, toroidal magnetic fields with highly ordered structures. At the same time, it disperses any coherent pulsations emitted by the NS. Consequently, PWNe are not expected to produce pulsed emission through the same shock emission mechanism described for J1023. In contrast, J1023 features a much more compact emission region located ≈ 100 km from the pulsar. At such close proximity, the interaction between the pulsar wind and the inflowing material from the accretion disk is more disruptive to the striped wind structure due to the higher density and turbulence of the accretion flow. This interaction likely results in a more tangled magnetic field at the shock region, which may be the main factor accounting for the lower polarization degree observed in J1023 compared to PWNe.

5 Conclusions

We have conducted the first multiwavelength polarimetric campaign of the tMSP PSR J1023+0038, using observations across the X-ray, optical, and radio bands. The results of our analysis can be summarized as follows:

- Timing analysis of the *IXPE* data revealed coherent X-ray pulsations at the NS spin period. The measured spin frequency suggests that the rotational evolution of the pulsar in its subluminescent X-ray state has remained largely unchanged compared to its behavior during the radio pulsar state.
- During the high mode, we detected polarized X-ray emission with a polarization degree of $(12 \pm 3)\%$ and angle of $-2^\circ \pm 6^\circ$ (1σ) in the 2–6 keV energy range. During the low mode, we derived an upper limit on the polarization degree of 26% at 90% c.l. We do not observe any significant variability in the polarization properties along the NS rotational phases or the binary orbital phases.
- Optical polarization measurements revealed a polarization degree of $(1.41 \pm 0.04)\%$, with a polarization angle aligning closely with that of the X-ray emission. This strongly suggests a common origin for

the polarized emission in both the optical and X-ray bands.

- No polarized emission was detected at radio wavelengths, down to 3σ upper limits on the polarization fraction of 9% in the high mode and 19% in the low mode.

- The SEDs of the polarized and pulsed fluxes align with a single power-law model across optical and X-ray energies, indicating that the polarized emission originates from the same processes driving the pulsed emission.

- The polarization degree in the high mode is higher than that seen in accreting NSs in LMXBs, indicating that standard accretion-powered emission mechanisms cannot fully explain the observed polarization. Additionally, scattering in an accretion disk wind alone is unlikely to account for the high polarization degree. Moreover, the lack of significant variability in the X-ray polarization properties across the pulsar rotational phases disfavors scenarios where the polarized signal arises as if the NS behaves like an isolated pulsar.

- Our findings support a scenario where the polarized emission is produced by synchrotron radiation at a shock formed by the interaction between the pulsar wind and the inner accretion disk. This gives insights into how the pulsar wind interaction with its environment shapes the observed emission properties.

- Our derived upper limits on the radio polarization fraction are consistent with the presence of a partially self-absorbed synchrotron-emitting compact jet during the high mode. During the low mode, the constraints align with expectations from synchrotron emission, considering potential depolarization effects.

These findings enhance our understanding of the complex interplay between accretion-powered and rotation-powered processes in tMSPs, and establish multiwavelength polarimetry as a crucial diagnostic tool for uncovering the physical mechanisms at work in these systems. Future observations, particularly those capable of measuring the polarization of pulsed emission, will be essential to further elucidate the nature of the emission processes in J1023 and similar objects.

Acknowledgments

We thank the *NICER* principal investigator, Keith Gendreau, for approving our Target of Opportunity (ToO) request and the operation team for executing the observations; we also thank the *Swift* deputy project scientist, Brad Cenko, and the *Swift* duty scientists and science planners, for making the *Swift*

ToO observations possible. We thank Alexandra Veledina and Juri Poutanen for fruitful discussions on the contribution of synchrotron emission from jets to polarization in X-ray binaries. We thank Alessio Marino for useful discussions on the spectral properties of low-mass X-ray binaries.

This research used data products provided by the *IXPE* Team (MSFC, SSDC, INAF, and INFN) and distributed with additional software tools by the High-Energy Astrophysics Science Archive Research Center (HEASARC), at NASA Goddard Space Flight Center (GSFC). This research is based on observations collected at the European Southern Observatory under ESO programme 113.27RE. *IXPE* is a joint US and Italian mission. *NICER* is a 0.2–12 keV X-ray telescope operating on the International Space Station, funded by NASA. The National Radio Astronomy Observatory is a facility of the National Science Foundation operated under cooperative agreement by Associated Universities, Inc.

M.C.B. acknowledges support from the INAF-Astrofit fellowship. F.C.Z. acknowledges support from a Ramón y Cajal fellowship (grant agreement RYC2021-030888-I). S.C. and P.D.’A. acknowledge support from ASI grant I/004/11/5. A.D.M. and F.L.M. are supported by the Italian Space Agency (Agenzia Spaziale Italiana, ASI) through contract ASI-INAF-2022-19-HH.0. A.P. and D.d.M. acknowledge financial support from the Italian Space Agency (ASI) and National Institute for Astrophysics (INAF) under agreements ASI-INAF I/037/12/0 and ASI-INAF n.2017-14-H.0 and from INAF ‘Sostegno alla ricerca scientifica main streams dell’INAF’, Presidential Decree 43/2018, from INAF ‘SKA/CTA projects’, Presidential Decree 70/2016. F.C.Z., S.Ca., P.D.’A., A.P., D.d.M. and G.I. acknowledge financial support from INAF-Fundamental research astrophysics project “Uncovering the optical beat of the fastest magnetised neutron stars” (FANS) and the Italian Ministry of University and Research (MUR) under PRIN 2020 grant No. 2020BRP57Z “Gravitational and Electromagnetic-wave Sources in the Universe with current and next-generation detectors (GEMS)”. AP acknowledges support from the Fondazione Cariplo/Cassa Depositi e Prestiti, grant no. 2023-2560. A.K.H. is supported by NSERC Discovery Grant RGPIN-2021-0400. D.M.R. and K.A. are supported by Tamkeen under the NYU Abu Dhabi Research Institute grant CASS. D.F.T. is supported by the grant PID2021-124581OB-I00 funded by MCIU/AEI/10.13039/501100011033 and 2021SGR00426. F.C. acknowledges support from the Royal Society through the Newton International Fellowship programme (NIF/R1/211296). G.I. is supported by the AASS Ph.D. joint research program

between the University of Rome “Sapienza” and the University of Rome “Tor Vergata” with the collaboration of the National Institute of Astrophysics (INAF). N.R. is supported by the European Research Council (ERC) under the European Union’s Horizon 2020 research and innovation programme (ERC Consolidator Grant “MAGNESIA” No. 817661) and the Proof of Concept “DeepSpacePulse” (No. 101189496). F.C.Z. and N.R. acknowledge support from grant SGR2021-01269 from the Catalan Government. This work was also supported by the Spanish program Unidad de Excelencia María de Maeztu CEX2020-001058-M and by MCIU with funding from European Union NextGeneration EU (PRTR-C17.I1).

Softwares

ASTROPY v.7.0, a community-developed core Python package for Astronomy [7]; CASA v.6.5 [27]; DAOPHOT [114]; DUST_EXTINCTION v.1.6 [56]; HEASOFT v.6.34 [92]; IPYTHON v.8.30 [102]; IRAF v.2.18, distributed by the National Optical Astronomy Observatory, which is operated by the Association of Universities for Research in Astronomy, Inc., under a cooperative agreement with the National Science Foundation (<https://iraf-community.github.io/>); IXPEOBSSIM v.31.0.3 [11], documented at <https://ixpeobssim.readthedocs.io/en/latest/>; MATPLOTLIB v.3.9.3, a Python library for publication-quality graphics [69]; NICERDAS v.13; NUMPY v.1.24.0 [62]; PANDAS v.2.2.2 [128]; PINT v.1.1 [86]; QUARTICAL v.0.2.3 [75]; SAOImageDS9 v.8.6, a tool for data visualization supported by the Chandra X-ray Science Center (CXC) and the High Energy Astrophysics Science Archive Center (HEASARC) with support from the James Webb Space Telescope Mission office at the Space Telescope Science Institute for 3D visualization [73]; SCIPY v.1.14.1 [125]; Swift Reduction Package (SRPAstro) v.4.9.0 (<https://pypi.org/project/SRPAstro/>); WSClean v3.4 [66]; XRONOS v.5.22 [113]; XSPEC v.12.14.0i [6].

Appendix

A Observations & data processing

The multiband data presented in this work were acquired by different space-borne and ground-based telescopes (Table 2). In the following, we describe the observations and the procedures adopted to process these data. In the following analyses, all timestamps are referenced to the barycenter of the Solar System using the Jet Propulsion Laboratory planetary development ephemeris DE440 [100] and the position derived from observations with the *Very Long Baseline Array* [36]: RA = $10^{\text{h}}23^{\text{m}}47^{\text{s}}69$ and decl. = $+00^{\circ}38'40.''8$ (Julian epoch date J2000.0; the uncertainties in both coordinates are $2 \mu\text{as}$).

A.1 IXPE

The *Imaging X-ray Polarimetry Explorer (IXPE)*, a joint mission between the National Aeronautics and Space Administration (NASA) and the Italian Space Agency (ASI), was launched on December 9, 2021. The observatory consists of three identical telescopes, each equipped with an X-ray mirror module assembly that uses grazing-incidence optics to focus X-rays onto a detector unit (DU). Each DU contains a polarization-sensitive gas-pixel detector (GPD) that measures linear X-ray polarization by imaging the tracks of photoelectrons produced by incoming X-rays absorbed in the special fill gas [12, 39]. The GPDs are capable of recording the arrival time of X-ray photons with a time resolution of $\approx 100 \mu\text{s}$ (for information on *IXPE*, see [111, 127]).

IXPE observed J1023 during two sessions: the first from 2024 May 29 at 12:32 UTC to 2024 June 2 at 18:12 UTC (MJD 60459.52 – 60463.76), and the second from 2024 June 3 at 21:15 UTC to 2024 June 14 at 14:58 UTC (MJD 60464.88 – 60475.62). The total exposure time per DU was $\simeq 675$ ks. Data processing was performed using the *ixpeobssim* package [11]. Both spectral and spectro-polarimetric analyses were conducted with *HEASoft* and the standard *FTOOLS*, utilizing the latest files in the *IXPE* Calibration Database (XRT version released on 2024 August 20, GPD version released on 2024 February 28).

Instrumental background in the photon event lists was reduced by applying the rejection algorithm by [40]⁷. Given the source faintness, background subtraction was also performed. Source and background photons were selected from the cleaned level-2 event data. Source photons were selected from a circular region with a $60''$ radius centered on the source, corresponding to roughly the 95% encircled energy

fraction for the point spread function of an on-axis source. The background was selected from an annular region with inner and outer radii of $150''$ and $300''$, respectively (Fig. 7). Even after background rejection, the background signal dominated above 6 keV. Consequently, the polarimetric analysis was restricted to the 2–6 keV energy band.

A.2 NICER

The *Neutron Star Interior Composition Explorer Mission (NICER)*; [52]) is a non-imaging X-ray observatory on board the International Space Station, with a field of view of ≈ 30 arcmin. The X-ray timing instrument of *NICER* consists of 56 co-aligned X-ray concentrator optics paired with silicon-drift detectors, 52 of which are currently operational. *NICER* is sensitive to photon energies in the 0.2–12 keV range, provides an effective collecting area of 1900 cm^2 at 1.5 keV, and offers a time resolution below 100 ns. During the *IXPE* campaign, we conducted a couple of *NICER* observations of J1023 as part of the director’s discretionary time (see Table 2 for a journal of the observations). These observations were aimed at guiding the selection of high and low-mode episodes in the *IXPE* dataset and were performed during orbit nighttime, ensuring high-quality data unaffected by the optical light leak caused by a damage of the thermal shield on one detector sustained in May 2023⁸. We reprocessed the data using the *NICER* Data Analysis Software (*NICERDAS*) version 13 distributed along with the *HEASoft* software package and the calibration products released on 2024 February 6. We calibrated and screened the raw unfiltered data and created level-2 cleaned event files using the *nicer12* pipeline with default settings. We extracted time series over the 0.5–10 keV energy range, binned at 10 s, using the *nicer13-1c* pipeline. To estimate the background level, we applied the *SCORPEON* model⁹ along with the latest geomagnetic data available at the time of analysis (see the yellow dashed lines in Fig. 9, bottom panel).

A.3 Swift

We performed a couple of observations with the *Neil Gehrels Swift Observatory (Swift)*; [51]) simultaneously with the VLA and VLT observations on 2024 June 4–5 (Table 2). During these observations, *Swift* utilized the X-ray telescope (XRT; [21]) in photon counting mode (readout time of 2.51 s) and the Ultra-Violet/Optical Telescope (UVOT; [106]) in event

⁸See https://heasarc.gsfc.nasa.gov/docs/nicer/analysis_threads/light-leak-overview/.

⁹https://heasarc.gsfc.nasa.gov/docs/nicer/analysis_threads/scorpeon-overview/

⁷<https://github.com/aledimarco/IXPE-background>

Table 2: Journal of the observations of J1023.

Telescope/Instr.	Obs./Prg. Id	Setup	Start – End time YYYY Mmm DD hh:mm:ss (UTC)	Exposure (ks)	Band
<i>IXPE</i> /DUs	03005599		2024 May 29 12:30:51 – 2024 Jun 14 14:57:45	675	2–8 keV
<i>NICER</i> /XTI	7034060107		2024 Jun 01 02:42:20 – 2024 Jun 01 21:36:39	4.3	0.5–10 keV
<i>Swift</i> /XRT/UVOT	00033012239	PC / Event mode	2024 Jun 04 22:14:59 – 2024 Jun 04 23:59:54	1.5	0.3–10 keV / <i>UVM2</i>
<i>Swift</i> /XRT/UVOT	00033012240	PC / Event mode	2024 Jun 05 01:23:09 – 2024 Jun 05 01:48:53	1.5	0.3–10 keV / <i>UVM2</i>
VLA	24A-476	B configuration	2024 Jun 04 23:10:31 – 2024 Jun 05 00:36:20	5.1	<i>C</i>
VLT/FORS2	113.27RE.001	Woll. prism + HWP	2024 Jun 04 23:34:37 – 2024 Jun 05 00:39:23	3.9	<i>R</i>
<i>Swift</i> /XRT/UVOT	00033012241	PC / Event mode	2024 Jun 06 02:39:12 – 2024 Jun 06 04:48:54	2.2	0.3–10 keV / <i>UVM2</i>
<i>NICER</i> /XTI	7034060108		2024 Jun 08 18:53:00 – 2024 Jun 08 22:17:30	1.4	0.5–10 keV

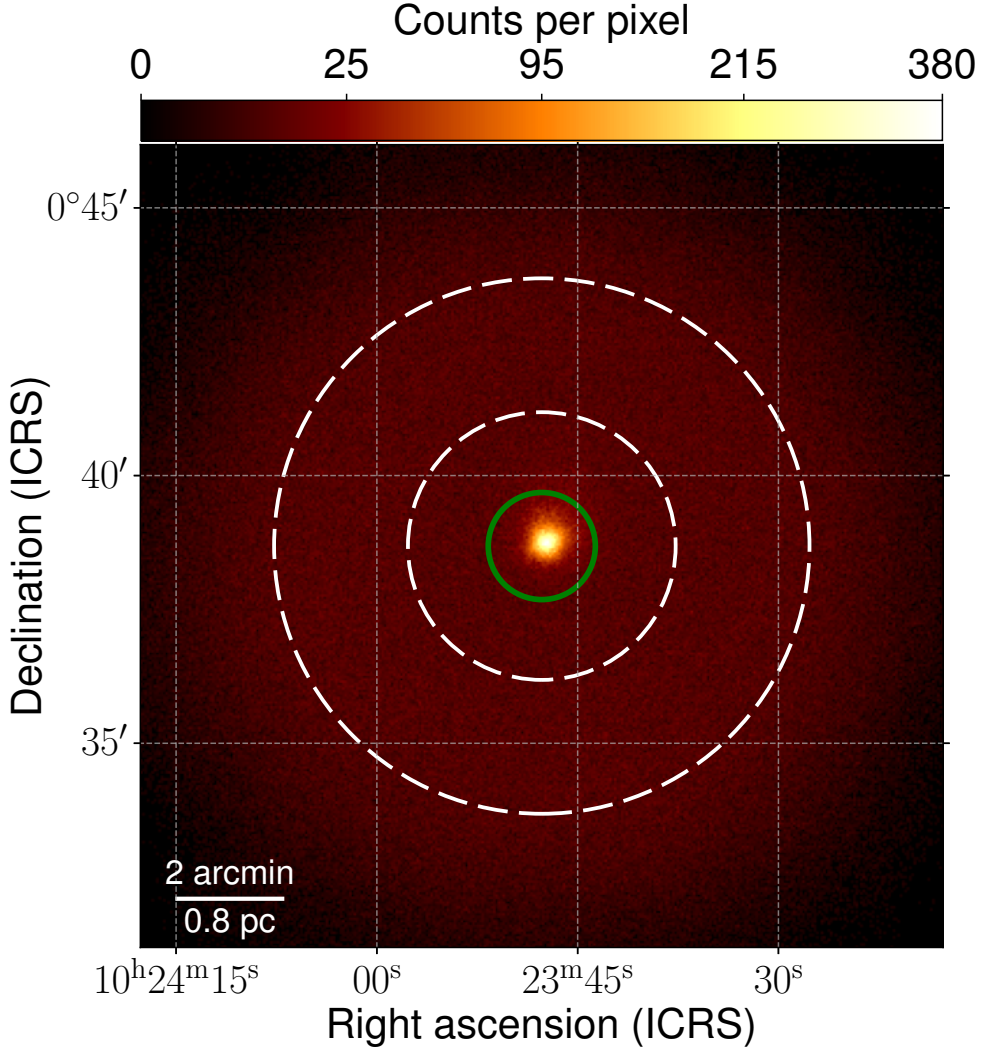


Figure 7: *IXPE* counts map of J1023 extracted by combining data from the three detector units after rejecting the background [40]. The map covers a 15' by 15' area centered on the radio position of J1023 [36]. Each spot is color-coded according to the number of counts per pixel at that position (the size of each pixel is 2.6'' by 2.6''). The green circle marks the region used to collect source photons, that is, a circle centered on the source position with a radius of 60''. The white dashed circles, also centered on the source position and with radii of 150'' and 300'', enclose the region adopted to estimate the background level. The conversion between angular and physical distances for the scale bar was calculated assuming a source distance of 1.37 kpc, as derived by [36]. Coordinates are reported in the International Celestial Reference System (ICRS) reference frame.

mode (readout time of 11 ms) with the UVM2 filter in place (central wavelength of 226 nm; full width at half maximum of 52.7 nm). Data were processed using the calibration files released on 2024 May 22 for XRT and on 2024 February 1 for UVOT.

After performing a standard screening of the XRT data, we collected source photons using a circular aperture with a radius of $47.2''$ centered on J1023 and estimated the background level using an annular region with inner and outer radii of $94.4''$ and $188.8''$, respectively. We then extracted background-subtracted time series in the 0.5–10 keV range, binned at 50 s (Fig. 9).

For the UVOT data, we used the `coordinator` and `uvotscreen` tools to convert raw coordinates to detector and sky coordinates, filter out hot pixels on the charge-coupled devices, and obtain cleaned event lists. We adopted a circular extraction region of radius $5''$ centered on the position of J1023 and a circular extraction region of radius $10''$ away from the source to collect source and background photons, respectively. We ensured that the extraction region was always centered on the source position in each observation snapshot, and extracted background-subtracted time series binned at 30 s using `uvotevtlc` (Fig. 9).

A.4 VLT

We observed J1023 with the FOcal Reducer/low dispersion Spectrograph 2 (FORs2; [2]) mounted on the Unit Telescope 1 (Antu) of the 8.2-m *Very Large Telescope* (VLT) at Paranal Observatory (Chile) in polarimetric mode (Table 2). The observations began on 2024 June 4 at 23:34:37 UTC (MJD 60465.982) and ended on 2024 June 5 at 00:39:23 UTC (MJD 60466.027), and were performed under photometric conditions (seeing $\simeq 0.3''$). A total of 56 images were acquired using the optical filter *R_SPECIAL* + 76 (*R*; central wavelength of 655 nm; full width at half-maximum of 165 nm), each with an exposure of 20 s, resulting in a total observing time of 3946 s, overheads included. A Wollaston prism was placed in the light path of the instrument, splitting the incident radiation into two orthogonally polarized beams (ordinary and extraordinary). A Wollaston mask was used to prevent these beams from overlapping on the CCD. Moreover, a rotating half-wave plate (HWP) was installed, allowing images to be captured at four distinct angles (Φ_i) relative to the telescope axis: $\Phi_i = 22.5^\circ(i-1)$, $i = 1, 2, 3, 4$. This step is critical to obtain polarization measurements because combining images taken at multiple (more than 2) angles is necessary to determine the level of linear polarization. Four sets of images were acquired with this setup, one for each angle of the HWP. This process

was repeated 14 times to obtain the entire dataset.

Images were processed by subtracting an average bias frame and dividing by a normalized flat field. Aperture photometry was performed using the `daophot` tool [114], using a 6-pixel aperture. Using Equations 1–2 of [9], we calculated the normalized Stokes parameters Q_{opt} and U_{opt} for the linear polarization. These parameters have not been corrected for instrumental contributions to the linear polarization. However, FORs2 routinely observes unpolarized standard stars to monitor instrumental polarization, and this has consistently remained very low (below 0.3%) across all bands over the past decade.

To estimate the degree and angle of linear polarization, we evaluated the parameter $S(\Phi)$ for each of the HWP angles, following [41] and references therein (see also [34, 9, 10]). $S(\Phi)$ describes the linear polarization along the Φ direction (e.g., $S(0^\circ) = Q_{\text{opt}}$), and it is defined as:

$$S(\Phi) = \left(\frac{f^o(\Phi)/f^e(\Phi)}{f_u^o(\Phi)/f_u^e(\Phi)} - 1 \right) \left(\frac{f^o(\Phi)/f^e(\Phi)}{f_u^o(\Phi)/f_u^e(\Phi)} + 1 \right)^{-1}. \quad (2)$$

Here $f^e(\Phi)$ and $f^o(\Phi)$ are the extraordinary and ordinary fluxes at a given angle Φ , respectively, and $f_u^e(\Phi)$ and $f_u^o(\Phi)$ are the corresponding fluxes for a non-polarized standard star in the field. The relationship between $S(\Phi)$, the polarization degree P_{opt} and the angle θ is given by:

$$S(\Phi) = P_{\text{opt}} \cos[2(\theta - \Phi)]. \quad (3)$$

The parameters P_{opt} and θ were determined through a two-step process: 1) maximizing the Gaussian likelihood function to provide an initial estimate for P_{opt} and θ ; 2) refining the estimates from 1) using a Markov Chain Monte Carlo (MCMC) procedure [67] (for further details on the algorithm, see [9, 10]). The best-fit values were obtained as the median of the marginal posterior distributions from the MCMC procedure. The uncertainties were estimated using the 16th to 84th percentiles of these distributions.

Since $S(\Phi)$ is calculated by normalizing with a non-polarized star in the field, the resulting value for the polarization degree obtained after fitting the $S(\Phi)$ curve is already corrected for instrumental effects. However, the polarization angle still requires correction using the Stokes parameters of a polarized standard star. To achieve this correction, we observed the star Vela 1-95 and measured its Stokes parameters to accurately determine its polarization angle. This measured angle was then compared to the tabulated value, resulting in a correction of $1.6^\circ \pm 0.7^\circ$ applied to the polarization angle of J1023. Finally, to correct for the interstellar contribution, instead of using only one non-polarized star, we used a group of reference stars in the same field as the target in

Equation 2, assuming these stars are non-polarized. This method allows the polarization degree of the target to be corrected for both instrumental and interstellar contributions. It is crucial to ensure that the chosen reference stars all exhibit the same polarization degree, which would be a good indicator of their intrinsic non-polarized nature (see e.g., [9]). Since the field of J1023 is relatively empty of optical sources, we could select only four comparison stars. However, these stars clustered very well together in the $Q_{\text{opt}} - U_{\text{opt}}$ plane, allowing us to determine the instrumental and interstellar polarization quite precisely in each image. We note that, as reported by [10], the maximum interstellar contribution to the linear polarization degree of J1023 is quite low ($P_{\text{opt,int}} < 0.52\%$), and comparable to the polarization measured for the instrument configuration.

A.5 VLA

We acquired radio observations of J1023 – simultaneous with the *IXPE* and VLT monitoring – using the *Karl G. Jansky Very Large Array* (VLA; Project ID 24A-476) radio interferometer. Our full observations, including both target and calibrator scans, began on 2024 June 4 at 23:00:00 UTC (MJD 60465.958) and ended on 2024 June 5 at 02:59:20 UTC (MJD 60466.125). The source underwent a bright multi-wavelength flare starting at $\simeq 00:36:00$ UTC on 2024 June 5 (MJD 60466.025); in this work, we only include the analysis of the pre-flare dataset (i.e., 2024 June 4 at 23:00:00 to 2024 June 5 at 00:36:00, with $\simeq 1.2$ hr on source).

We observed in C-band (central frequency of $\simeq 6$ GHz) using the 3-bit sampler, which breaks the total un-flagged bandwidth of 4096 MHz into 32 spectral windows, each comprised of 64 2 MHz frequency channels. We used 3C286 as the flux and bandpass calibrator, J1024–0052 as the nearby complex gain calibrator (i.e., the secondary), and the unpolarized source, J1407+2827, as the leakage calibrator. The target monitoring of J1023 was broken into $\simeq 9$ -min scans, with two 1-min secondary scans bookended each target scan.

We flagged and calibrated the parallel-hand visibilities with the Common Astronomy Software Applications package (CASA) VLA pipeline [26]. After the pipeline processing was completed, we inspected the visibilities, removing residual radio frequency interference (RFI) through a combination of manual editing and CASA auto-flagging algorithms (i.e., `rflag` and `tfcrop`). After the parallel-hand calibration (which is only sufficient for Stokes I) we calibrated the cross-hand visibilities following the procedure outlined in the VLA tutorials¹⁰.

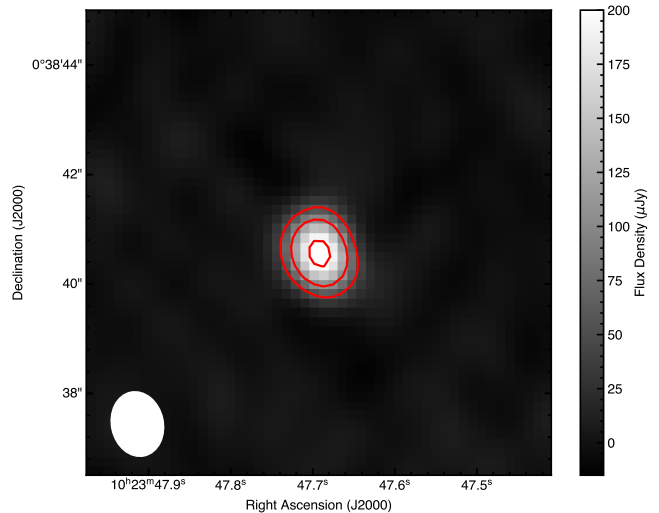


Figure 8: 6-GHz VLA image of the sky region around J1023, color-coded according to the values of the flux density at each position (as indicated by the color bar on the right). To aid visualization, contour levels are indicated in red, and are drawn at intervals of $10\times$, $20\times$, $40\times$ the image plane rms noise. The white ellipse in the bottom-left corner represents the shape and size of the synthesized beam, where the major axis is $1.15''$, the minor axis is $0.91''$, and the major axis is located at a position angle of 12.2° measured from North towards East.

We created Stokes $IQUV$ images with the `WSClean` imager [94]; `WSClean` is a `CLEAN`-based deconvolution algorithm [66] that removes sampling artefacts from interferometric images. To produce our final data products, we first performed a shallow unmasked deconvolution of the full $10'$ field of view (FOV), i.e., we created preliminary images. We made a deconvolution mask using the unmasked Stokes I image and, with the mask, re-imaged the target field. Adopting the masked image as a model, we performed phase-only self-calibration on the target visibilities with the software package `QuartiCal` [75]. We then refined the mask and repeated the imaging and self-calibration procedure a second time. In the FOV of J1023, there exists, among other fainter background sources, a bright radio Galaxy (J102358.2+003826) at an angular offset of $\sim 3''$. Using the self-calibrated model, we subtract out the visibilities for the background sources, allowing for narrow FOV images that are minimally affected by aliasing.

During the VLA observations, J1023 had an average flux density of $\simeq 240 \mu\text{Jy}$ at 6 GHz. We created two sets of $IQUV$ images using our background-

[//casaguides.nrao.edu/index.php/CASA_Guides:Polarization_Calibration_based_on_CASA_pipeline_standard_reduction:_The_radio_galaxy_3C75-CASA6.5.4](https://casaguides.nrao.edu/index.php/CASA_Guides:Polarization_Calibration_based_on_CASA_pipeline_standard_reduction:_The_radio_galaxy_3C75-CASA6.5.4)

¹⁰The tutorial can be found here: https://casaguides.nrao.edu/index.php/CASA_Guides:Polarization_Calibration_based_on_CASA_pipeline_standard_reduction:_The_radio_galaxy_3C75-CASA6.5.4

subtracted visibilities. First, we broke the observations into 1-minute imaging intervals, allowing us to (temporally) resolve the radio variability. The 1-minute images revealed that J1023 underwent a mini-flare lasting $\simeq 8$ min and reaching a maximum flux density of $\simeq 500 \mu\text{Jy}$. We created four additional images that combined multiple target scans to get deeper polarization limits, sacrificing temporal resolution for higher signal-to-noise. The deep imaging time intervals were 23:10:31–23:52:25 UTC (June 4), 23:52:25–00:00:22 UTC (June 4 to June 5) and 00:00:22.5–00:36:20 UTC (June 5); these intervals correspond to the times before the mini-flare, the mini-flare, and the times after the mini-flare. The fourth image combined the times before and after the mini-flare.

In each imaging interval, `WSClean` outputted 16 channelized images (evenly spaced in frequency) and a single frequency-averaged ‘Multi-Frequency-Synthesis’ (MFS) image. We measure the target’s Stokes I flux density from the MFS image, using the `CASA` task `imfit`. `imfit` models the intensity distributions as an elliptical Gaussian; given that J1023 is a point source, we enforce a synthesized beam-shaped Gaussian fit. We quantified the 1σ uncertainty on the flux density with the root-mean-square (RMS) noise extracted from a nearby source-free region. Using the `CASA` task `imstat`, we measure the RMS using a circular aperture with an area equal to $\simeq 100\times$ synthesized beam area. Additionally, for MFS images where J1023 was detected at $>20\sigma$ (corresponding to $>5\sigma$ in each channelized image), we calculate the intra-band power-law spectral index from channelized flux densities (using `scipy.curve_fit`) α , which describes how the flux density F_ν varies with observing frequency ν as $F_\nu \propto \nu^\alpha$. We found that α remains nearly constant during the high-mode episodes that precede (H1) and follow (H2) the low mode, but decreases during the low mode (L). Specifically, we obtain $\alpha_{\text{H1}} = 0.50 \pm 0.13$, $\alpha_{\text{H2}} = 0.51 \pm 0.16$ and $\alpha_{\text{L}} = -0.03 \pm 0.25$.

Lastly, we produced linear polarization intensity images ($P_{\text{radio}} = \sqrt{Q_{\text{radio}}^2 + U_{\text{radio}}^2}$) for each imaging interval but did not detect any polarized emission. As a result, we calculate 3σ ($\simeq 99.7\%$) percent upper-limits from the P -images following the prescription by [120]. We obtain $P_{\text{radio,H1}} < 10\%$, $P_{\text{radio,H2}} < 14\%$ and $P_{\text{radio,L}} < 19\%$. By stacking high-mode data, we obtain $P_{\text{radio,H}} < 9\%$.

B Selection of Emission Modes in the *IXPE* Dataset

The top panel of Fig. 9 shows the time series for the *IXPE* observations, whereas the middle and bottom

panels show the six time intervals where there was overlap between *IXPE* and *NICER* observations, totaling $\simeq 2$ ks. In each interval, the average background intensity in the *NICER* dataset was $\simeq 10$ – 15% of the total emission (source plus background), except for the last time segment, where the emission was consistently faint, and the background intensity accounted for $\simeq 30\%$ of the total emission. Nonetheless, during these overlapping time intervals, we did not observe any significant variation in the background level possibly correlated with mode-switching episodes, except for the fifth interval, where a slightly enhanced background level was detected at the exit of a low mode. This increase in the count rate should be approached with caution. Overall, we detected four low modes in the *NICER* data that were covered by *IXPE*: one in the second time segment, one in the third, one in the fifth, and one throughout the entire duration of the sixth segment.

To select the appropriate thresholds for the count rates in order to select the distinct emission modes in the *IXPE* data, we proceeded as follows. Over the past decade, the net count rate observed in all previous observations of J1023 carried out by the European Photon Imaging Cameras (EPIC) on board *XMM-Newton* decreased by a factor of approximately six during the low mode compared to the average net count rate (e.g., [18, 33]). The average count rate of J1023 measured by *IXPE* after combining data from the three DUs is $\simeq 0.09 \text{ counts s}^{-1}$, with about 30% of this rate contributed by the background level. Consequently, during low-mode episodes, typically only 0 or 1 net photon from the source, plus 3–4 photons from the background, would be detected by *IXPE* in 100-s time bins. In fact, during the low modes covered by *NICER*, the highest count rate measured in the *IXPE* time series binned at 100 s is $0.05 \text{ counts s}^{-1}$ (summing up the source and background contributions). We then classified time intervals in the *IXPE* light curves as low modes whenever the count rate in the 100-s binned time series was less than or equal to $0.05 \text{ counts s}^{-1}$. This criterion resulted in the selection of about 182 ks of low-mode data, which corresponds to about 27% of the total exposure time. This value is consistent with the fraction of time that J1023 was detected in the low mode in previous observations [5, 18, 33].

To differentiate between high and flaring modes, we extracted the distribution of count rates above $0.05 \text{ counts s}^{-1}$ and modeled it using two Gaussian functions. We then classified a 100-s time bin as a flare mode if its count rate was at least 4 standard deviations above the mean count rate of the Gaussian distribution representing the high mode, which corresponds to a threshold of $\approx 0.2 \text{ counts s}^{-1}$ (Fig. 10).

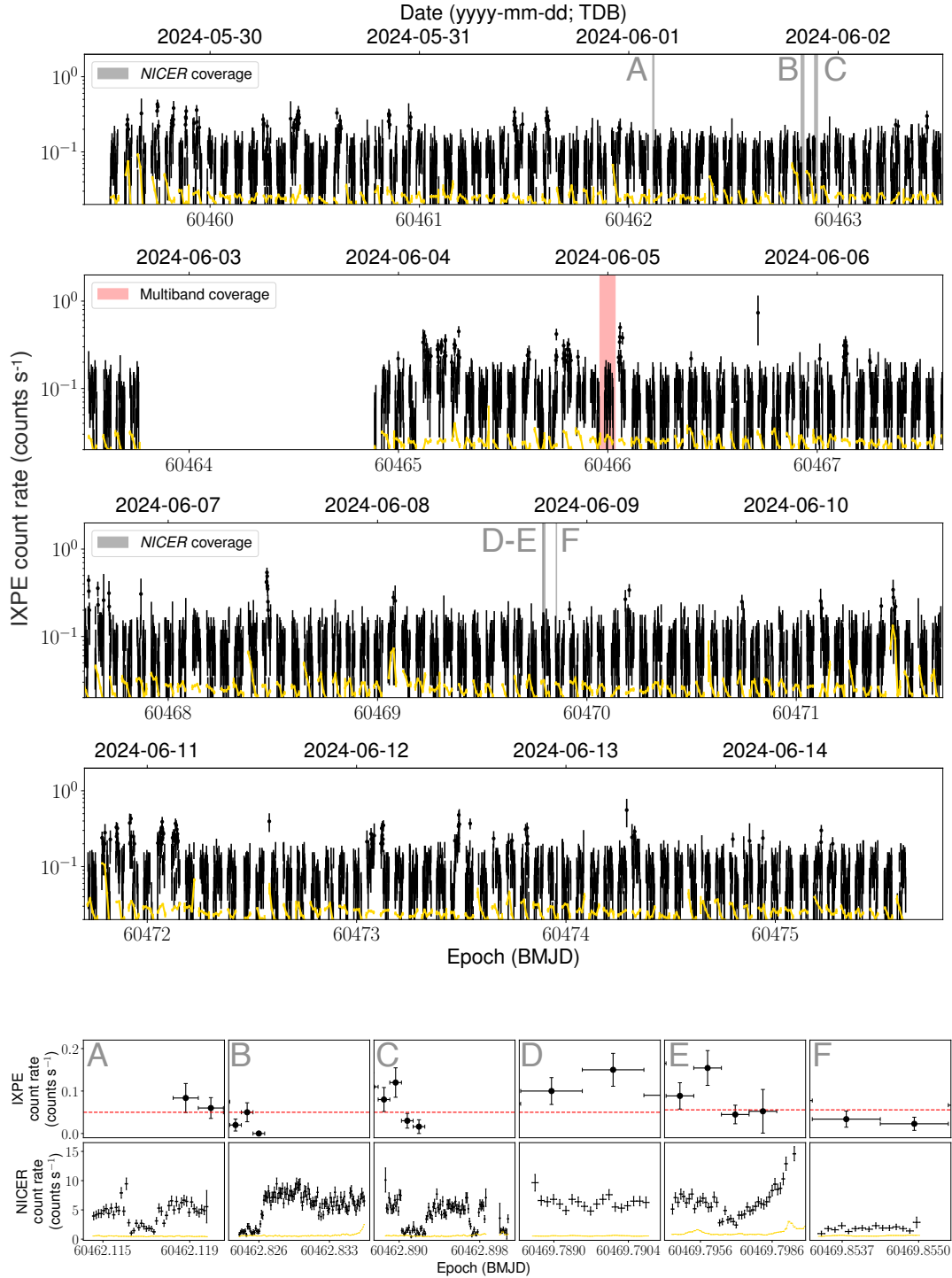


Figure 9: Top: *IXPE* time series extracted from the source region and binned at a 100-s resolution (black) and from the background region and binned at 1 ks (yellow). Both time series were extracted by combining data from the three detector units, with the background time series rescaled to account for the area differences between the source and background extraction regions. The gaps in the time series correspond to time intervals when J1023 was obscured by the Earth. The vertical gray stripes mark the six-time intervals of the simultaneous *NICER* observations, while the magenta-shaded area represents the time interval covered by VLT and VLA observations in the optical and radio bands. Bottom: *IXPE* and *NICER* time series for each overlapping time interval, with the *NICER* data binned at 10 s. The horizontal red dashed lines in the middle panels indicate the count rate threshold adopted to differentiate between high and low mode episodes in the *IXPE* dataset, while the yellow dashed lines in the bottom panels depict the *NICER* background level estimated using the *SCORPEON* model. The final part of the fifth time segment of the *NICER* dataset is characterized by enhanced background level. Therefore, caution should be exercised in interpreting the corresponding increase in the count rate. BMJD stands for Barycentric Modified Julian Date, TDB for Barycentric Dynamical Time.

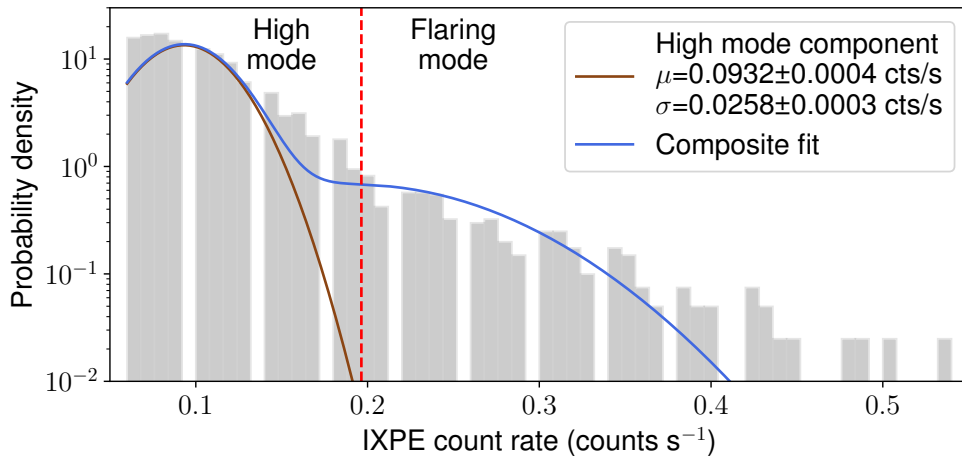


Figure 10: Probability density function of *IXPE* count rates and its modeling. The gray filled bins represent the distribution of count rates extracted from time series binned at 100 s and filtered to include only intervals where the count rates exceeded $0.05 \text{ counts s}^{-1}$ (thereby discarding low-mode episodes). The gaps between some of the bins in the distribution result from the limited number of photon counts detected by *IXPE* in each time bin. The distribution was fit with two Gaussian functions. The blue line represents the probability density function (PDF) of the composite model that best fits the observed data. The brown curve represents the PDF of the Gaussian component associated with the high mode. The mean (μ) and standard deviation (σ), along with their $1\text{-}\sigma$ uncertainties, are provided in the legend. The vertical red dashed line marks the threshold adopted to identify the flaring mode, set at $0.196 \text{ counts s}^{-1}$, which corresponds to 4σ above the mean of the high mode component. The vertical axis is plotted on a logarithmic scale to highlight the tail of the distribution at higher count rates in the flaring mode.

This approach resulted in the selection of ≈ 20 ks of flaring-mode data, which represents $\approx 3\%$ of the total duration of the *IXPE* observations. This percentage is again consistent with the fraction observed in previous observations [5, 18, 33].

C Timing Analysis of the *IXPE* Dataset

Previous studies have shown that coherent X-ray pulsations at the NS spin period in J1023 are detected only during the high mode [5, 71, 98, 70]. Hence, to search for a pulsed signal in the *IXPE* data, we retained only source photons collected during the high mode, and restricted the analysis to photons in the energy range 2–6 keV. We corrected the photons’ arrival times for the motion of the pulsar along the binary orbit, setting the orbital period and the projected semi-major axis of the circular orbit to the values reported by [3], $P_{\text{orb}} = 17115.5216592 \text{ s}$ and $a \sin i/c = 0.343356 \text{ light-seconds}$ (the uncertainties in these parameters are of the order 10^{-7} s and $10^{-6} \text{ light-seconds}$, respectively). To measure the epoch of passage of the pulsar at the ascending node of the orbit (T_{asc}), we performed an epoch folding search on the *IXPE* dataset around the spin frequency value expected according to the previously measured secular evolution [71, 22], sam-

pling each spin cycle in 16 phase bins. We used a grid of T_{asc} values centered on the value predicted according to the long-term evolution measured by [70], $T_{\text{asc}}^{\text{pred}} = 60461.97948(6) \text{ MJD}$, with a spacing of 0.2 s. We recovered the coherent signal with an epoch folding variance of $S = 103$ (corresponding to a single-trial false alarm rate of $p = 3.5 \times 10^{-15}$) at a spin frequency of $\nu = 592.42146705(9) \text{ Hz}$ and $T_{\text{asc}} = 60461.979580(14) \text{ MJD}$. The uncertainty on the spin frequency was evaluated following [80], while that on T_{asc} was taken as the half-width at half-maximum of the Gaussian fit to the pulse variance distribution. The timing model, compatible with the *Tempo2* [65] and *PINT* [86] pulsar timing packages, will be made available at Zenodo.

The top panel of Fig. 13 shows the *IXPE* background-subtracted double-peaked pulse profile. We calculate the fractional RMS variability amplitude (F_{var}) of the pulsed signal following the method by [121] and obtain $F_{\text{var}} = 8.1\% \pm 0.8\%$. This value is consistent within the uncertainties with those derived in previous studies [5, 71, 98].

We obtained compatible results by analysing 0.5–6 keV *NICER* data in the high mode taken on 2024 June 1. The timing parameters had slightly larger uncertainties due to the lower number of photons recorded ($\approx 1.9 \times 10^4$) compared to *IXPE* ($\approx 2.2 \times 10^4$) and the uneven coverage.

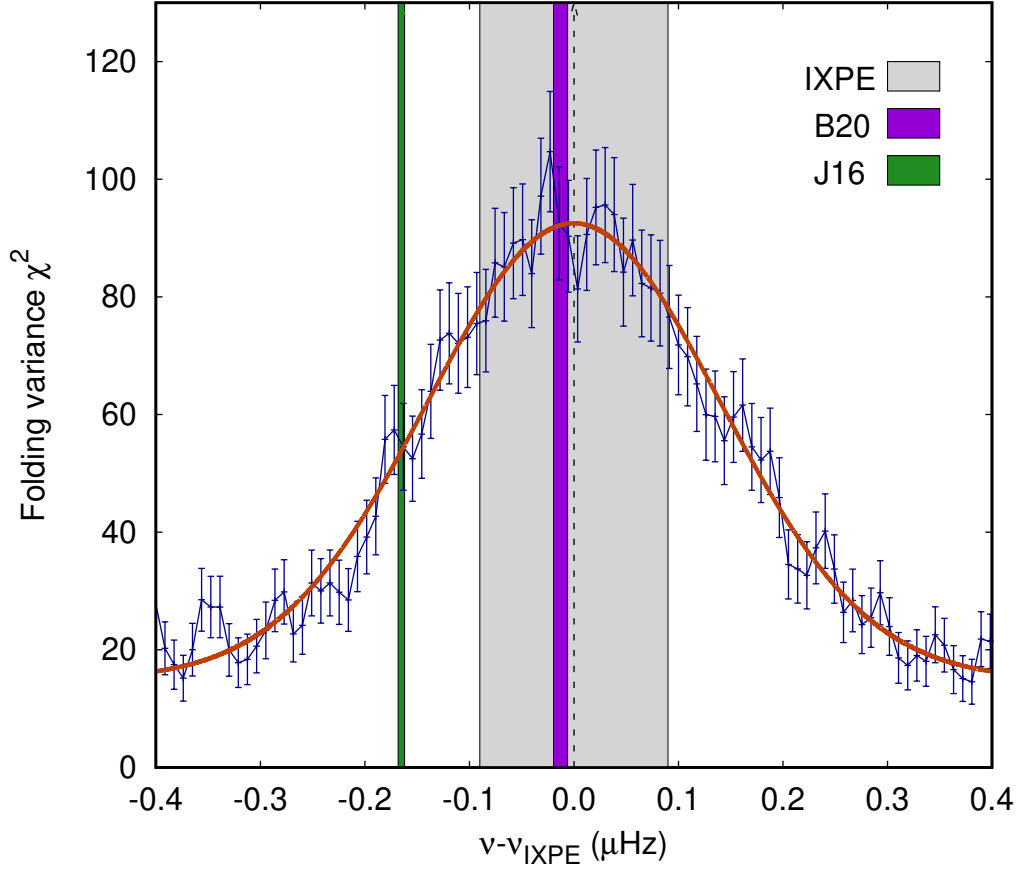


Figure 11: Variance distribution for the coherent pulsations of J1023 detected by *IXPE*. The distribution is derived from an epoch folding search of data filtered for the high mode in the 2–6 keV energy range. The folding variance is plotted against the frequency deviation from the *IXPE*-measured spin frequency, $\nu_{IXPE} = 592.42146705(9)$ Hz, marked with a vertical dashed line. The red solid curve marks the best-fitting Gaussian function to the pulse variance distribution. The shaded areas indicate the uncertainty regions around the spin frequency measured by *IXPE* (gray) or those predicted by extrapolating the solutions reported by [22] (B20; purple) and [71] (J16; green) to the epoch of the *IXPE* observation.

Table 3: Timing parameters for J1023. Numbers in parentheses indicate the uncertainty on the last quoted digit(s).

Dataset and model summary	
Pulsar name	J1023+0038
MJD range	60459.5257–60475.6217
Data span (d)	16.096
Solar system ephemeris	DE440
Time unit	TDB
Parameters	
POSEPOCH, Reference epoch for position (MJD)	55000.00
RAJ, Right Ascension (J2000)	10 ^h 23 ^m 47.687198 ^s
DECJ, Declination (J2000)	+00°38′40.84551″
F0, Spin frequency (Hz)	592.42146705(9)
PB, Orbital period (d)	0.1980963155
A1, Projected semi-major axis of pulsar orbit (lt-s)	0.343356
TASC, Epoch of ascending node (MJD)	60461.979580(14)

The spin frequency measured from *IXPE* data is compatible within the uncertainties with the value predicted from the quasi-coherent timing solution derived from optical data by [22] ($\nu_{\text{exp,B20}} = 592.421467042(7)$ Hz), who found a spin down rate very close to the value observed when J1023 was detected as a radio pulsar before the state transition occurred in 2013. On the other hand, it differs by 160 ± 90 nHz from the value predicted by [71] ($\nu_{\text{exp,J16}} = 592.421466890(3)$ Hz), who reported a spin-down rate about 20% faster (Fig.11). Even though this difference is still compatible within a 3σ c.l., our measurement tends to favor a scenario in which the rotational evolution of the pulsar in the subluminescent X-ray state has remained largely unchanged compared to its behavior during the radio pulsar state.

D X-ray Polarimetric Properties

D.1 Model-independent Analysis

We first perform a model-independent polarimetric analysis of the *IXPE* data using the formalism outlined by [76] implemented in the *ixpeobssim* package [11] under the *pcube* algorithm in the *xpbin* routine. We compute the normalized, background-subtracted Stokes parameters $q_X = Q_X/I_X$ and $u_X = U_X/I_X$, where Q_X , U_X and I_X are the Stokes parameters. From these, we derive the polarization degree $P_X = \sqrt{q_X^2 + u_X^2}$ and polarization angle (also referred to as the electric vector position angle) $PA_X = \frac{1}{2} \arctan(u_X/q_X)$, measured counterclockwise from the North celestial pole toward the East. Hereafter, uncertainties are given at the 68.27% c.l. unless noted otherwise.

In the 2–6 keV energy band, we obtain an MDP of 11% at a 99% c.l. and $P_X = (7 \pm 4)\%$. The polarization in the 2–3 keV energy range is consistent with zero within 1σ , while low-significance polarization is consistently detected across the 3–4, 4–5, and

5–6 keV energy ranges (Fig. 2). In the 3–6 keV range, we find an MDP of 15% and measure a polarization degree that exceeds this threshold, $P_X = (16 \pm 5)\%$, with $PA_X = -7^\circ \pm 9^\circ$. To assess the significance of this detection, we use the ratio of the polarization degree to its standard deviation, $P_X/\sigma_{P_X} = 3.2$, as the primary indicator of statistical significance¹¹. Using the χ^2 distribution for two dofs, we calculate a confidence level (c.l.) of 99.4%.

Applying the same analysis to high-mode data, we obtain an MDP of 12% in the 2–6 keV range, with $P_{X,H} = (7 \pm 4)\%$ and $PA_{X,H} = -9^\circ \pm 18^\circ$. The energy-resolved analysis corroborates the results from the entire data set (Fig. 3). In the 3–6 keV range, we find an MDP of 16% and $P_{X,H} = (13 \pm 5)\%$, with $PA_{X,H} = -1^\circ \pm 11^\circ$.

For low-mode and flaring-mode data, the significance was too low for a reliable polarimetric analysis. For the low mode, we obtained an MDP of 50% and $P_{X,L} < 26\%$ at a 90% c.l.. For the flaring mode, we derived an MDP of 30% and $P_{X,F} < 28\%$ at a 90% c.l..

D.2 Spectro-polarimetric Analysis

To enhance the significance of the polarimetric measurements, we conducted a spectro-polarimetric analysis of the data as outlined by [116], following the weighted analysis method prescribed by [38], where each photoelectron track recorded by the DUs is assigned a weight based on its ellipticity. We extracted the Q_X , U_X and I_X spectra for each DU using the *xpbin* tool’s PHA1 algorithms in *ixpeobssim*, applying a constant energy binning of 200 eV. We assigned the response matrices 20240701_alpha075 available in the calibration database and computed modulation response functions and ancillary response files using *ixpecalcarf*.

Previous observations have shown that the X-ray spectrum of J1023 during its high mode is well described by an absorbed power-law model (e.g., [18, 33, 24]). Hence, the adopted model includes a power-law component corrected for interstellar medium effects using the Tübingen-Boulder model [130] with photoelectric cross-sections by [124], convolved with an energy-independent polarization model. To account for potential discrepancies between the effective areas of the different DUs, we also included a cross-normalization constant, which was fixed at unity for DU1 to serve as the reference, and allowed to vary for DU2 and DU3. Thus, the final model employed within the *XSpec* spectral fitting package [6] is `const × TBabs × powerlaw × polconst`. We fit this model simultaneously to the Stokes energy

¹¹https://heasarc.gsfc.nasa.gov/docs/ixpe/analysis/IXPE_Stats-Advice.pdf

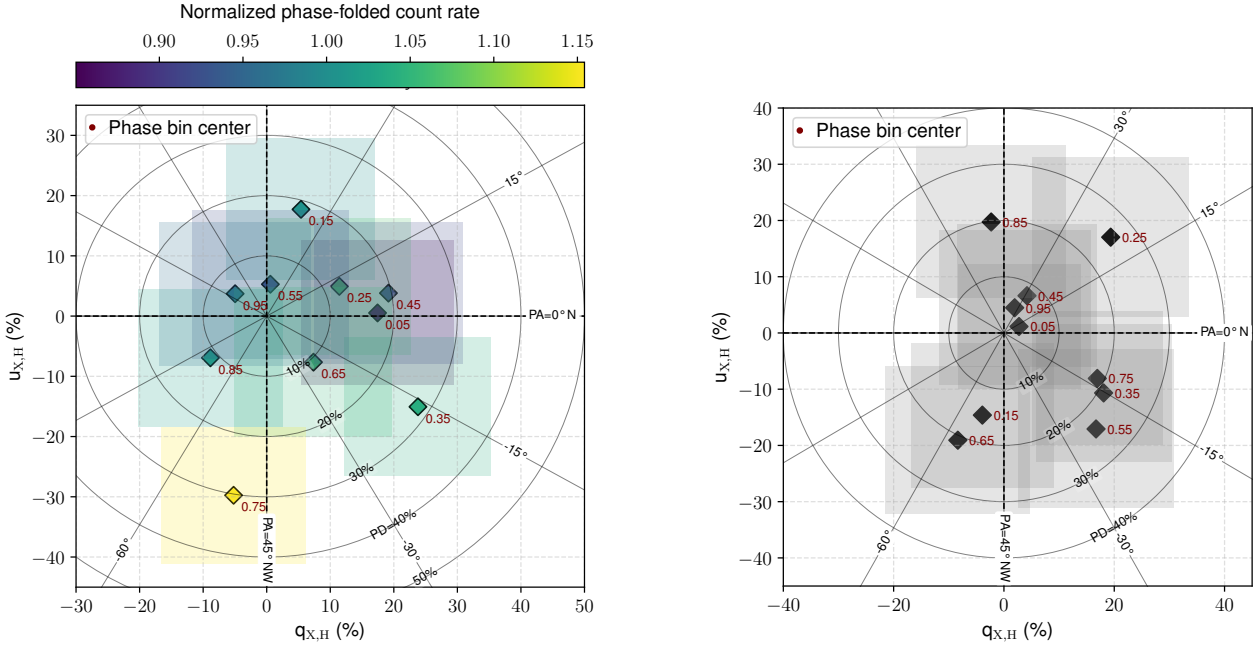


Figure 12: Normalized and background-subtracted Stokes parameters in the high mode in the 2-6 keV energy in distinct pulsar rotational phase bins (left) and binary orbital phase bins (right). The results are derived from an unbinned analysis of the combined data from all three DUs. Each diamond represents the mean value for a phase bin, with the center of each phase bin highlighted in bordeaux. The corresponding shaded square area shows the 1σ standard deviation. The circles give the contours of constant polarization degree while the radial lines correspond to constant polarization angle. In the left panel, both diamonds and square areas are color-coded based on the normalized background-subtracted count rate in the corresponding pulse profile phase bin.

spectra of all DUs in the 2–6, 2–3 and 3–6 keV energy ranges using the forward-folding, maximum likelihood procedure implemented in `XSpec`.

Observations over the past decade have shown that the X-ray spectral shape of J1023 has remained remarkably stable throughout this time span [18, 33, 24]. Hence, during the fitting process, we fixed the absorption column density (N_{H}) and power-law photon index (Γ_X) at the values measured in previous works: $N_{\text{H}} = 2.8 \times 10^{20} \text{ cm}^{-2}$, $\Gamma_X = 1.69$. All other parameters were allowed to vary. The results are summarized in Table 1 and are consistent with those derived from the model-independent analysis. Figure 4 shows the confidence contours for the measurements of $P_{\text{X,H}}$ and $PA_{\text{X,H}}$ obtained over distinct energy bands, drawn using the `steppar` command in `XSpec`.

It is noteworthy that previous analyses of the distributions of mode durations extracted from observations carried out by *XMM-Newton* EPIC [5] show that $\simeq 40\%$ of low-mode episodes last less than 100s. This implies that our method for selecting the emission modes inherently misses short low-mode episodes totaling $\simeq 10\%$ of the total duration of the *IXPE* observations. According to [10], the emission during the low mode is expected to be polarized to a lower extent compared to the high mode

due to the much smaller contribution of the shock emission. Even in the most extreme case where the low-mode emission is fully unpolarized, the X-ray polarization degree during the high mode selected using our criteria would be enhanced by a factor of $1 + \frac{0.1 \times CR_{\text{low}}}{CR_{\text{high}}} \simeq 1.01$ [40]. Here, CR_{low} and CR_{high} represent the background-subtracted count rates in the *IXPE* band in the low and high modes, respectively. This small increase, equivalent to about 0.2% in the polarization degree, is within the margin of the measurements uncertainties, meaning that as a matter of fact the intrinsic X-ray polarization degree of the high-mode emission remains unchanged within the limits of our observations.

D.3 Phase-Resolved Analyses

We conducted both rotational and orbital phase-resolved analyses of the X-ray polarimetric properties. Using the `photonphase` tool in the `PINT` software package [86], we computed the rotational and orbital phases of each photon collected in the high mode in the 2–6 keV energy range by *IXPE*, based on the timing model derived from the *IXPE* data analysis. For each analysis, we split the data into 10 phase bins, and calculated the Stokes parameters for each bin using the `pcube` algorithm within `ixpeobssim`,

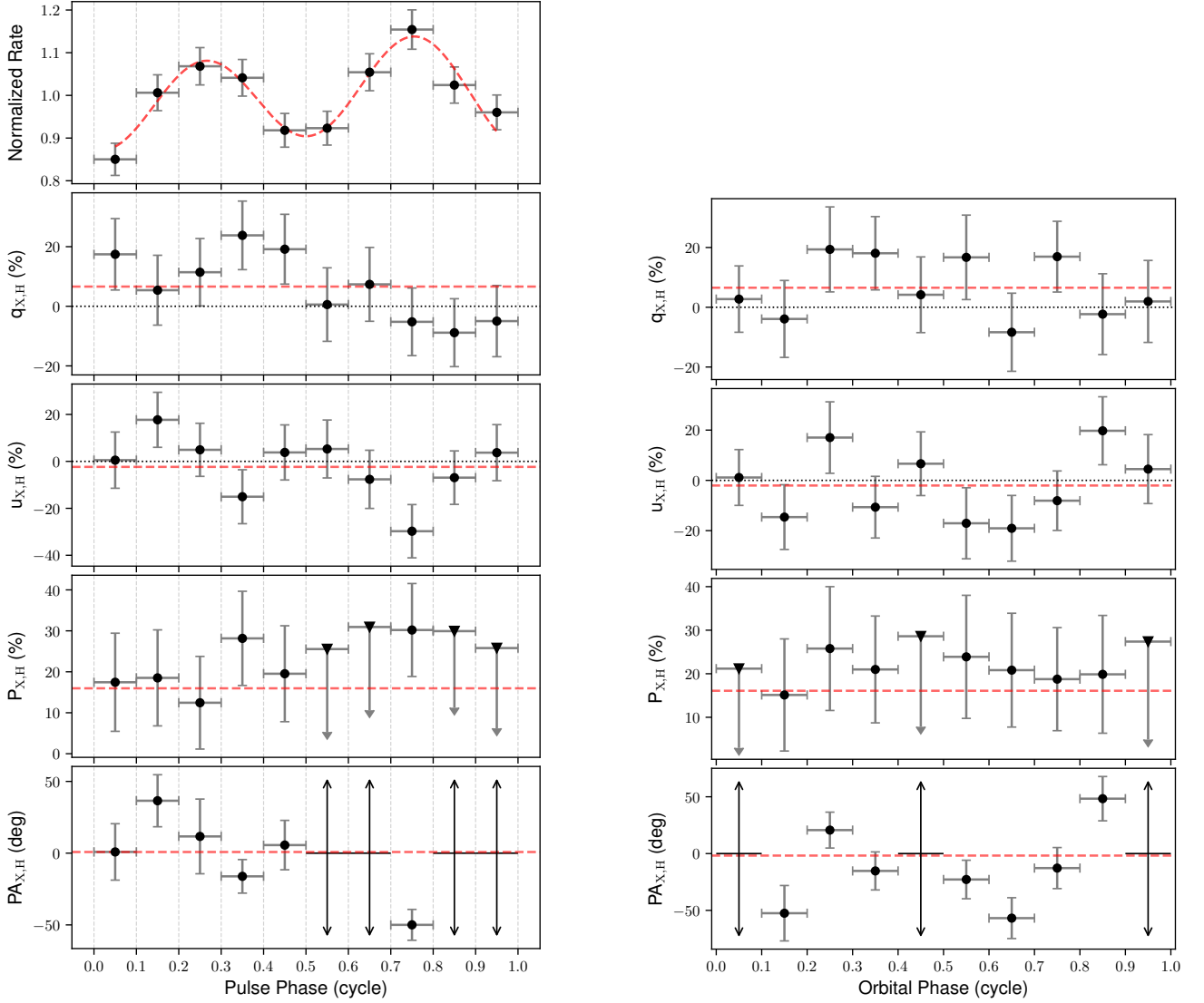


Figure 13: Rotational (left) and orbital (right) phase dependence of the 2–6 keV normalized flux and polarization properties of J1023 in the high mode. From top to bottom, the left panel shows the pulse profile normalized to the average background-subtracted count rate as well as the normalized Stokes parameters q_X and u_X , the $P_{X,H}$, and the $PA_{X,H}$ sampled in 10 phase bins as a function of the rotational phase and after background subtraction. From top to bottom, the right panel shows the normalized Stokes parameters q_X and u_X , the $P_{X,H}$, and the $PA_{X,H}$ sampled in 10 phase bins as a function of the orbital phase and after background subtraction (here phase 0 corresponds to the time of passage of the pulsar through the ascending node of the orbit). In both panels, upper limits are indicated with arrows and are reported at the 90% c.l. for bins compatible with null values at the 68% c.l.. The $PA_{X,H}$ values are unconstrained for bins where upper limits on the $P_{X,H}$ have been derived. The red dashed line in the top left panel indicates the best-fitting model comprising the fundamental and first harmonic components of the spin signal, whereas the red horizontal dashed lines in all other panels indicate the mean of the plotted polarization parameters. q_X and u_X are statistically consistent with remaining constant across the phases (see text for more details).

following the same model-independent procedure described above and applying background subtraction.

Figure 12 shows the Stokes parameters in distinct pulsar rotational phases (left) and binary orbital phases (right). The left panel of Figure 13 displays the Stokes parameters, $P_{X,H}$ and $PA_{X,H}$ as a function of the rotational phase. We do not measure statistically significant (anti-)correlations between the normalized rate and the Stokes parameters. Specifically, Spearman rank and Kendall tau correlation analyses between the normalized rate and $q_{X,H}$ yielded coefficients of -0.25 (p-value = 0.49) and -0.16 (p-value = 0.60), respectively. Similarly, correlation analyses between the normalized rate and $u_{X,H}$ resulted in coefficients of -0.47 (p-value = 0.17) and -0.33 (p-value = 0.22), respectively. Constant fits to the q_X and u_X values produced χ^2 values of 8.5 and 11.8 for 9 dof, respectively. The right panel of Figure 13 shows the Stokes parameters, $P_{X,H}$ and $PA_{X,H}$ as a function of the orbital phase. Similarly, no significant variability was observed in q_X and u_X , with constant fits yielding χ^2 values of 5.6 and 9.8 for 9 dof, respectively.

E Optical Properties

All VLT observations resulted in significant detections (above 3σ), with a mean linear polarization level of $P_{\text{opt}} = (1.38 \pm 0.04)\%$ (1σ). This value aligns with previous results obtained in the same band [8, 10], although it is slightly higher. The polarization angle is well-constrained, with a mean value of $PA_{\text{opt}} = -4.1^\circ \pm 0.7^\circ$ (1σ ; measured after correcting for the polarization angle of the standard star). This value is consistent with that reported by [10], although our measurements are significantly more precise.

In addition to the polarimetric analysis, it is also possible to extract and calibrate fluxes to build a light curve. If we assume the flux loss is negligible, the sum of the intensities measured in both the ordinary and extraordinary beams for each image gives the total flux from the target. Therefore, we summed the ordinary and extraordinary fluxes for each image of J1023, as well as for two isolated field stars with R2 magnitudes listed in the USNO B1 catalogue [91]. The resulting flux was then calibrated against the flux of the reference stars.

Figure 1 shows the time evolution of the magnitude, P_{opt} and PA_{opt} . To quantify the intrinsic variability amplitude of the light curve, we computed the excess variance $ExcessVar = \sigma_m^2 - \sigma_{m,\text{err}}^2$, where σ_m is the standard deviation of the magnitudes and $\sigma_{m,\text{err}}^2$ is the mean square measurement error in magnitudes. We obtain $ExcessVar \simeq 0.02 \text{ mag}^2$, indicating moderate variability.

Table 4: Optical polarimetric measurements. All uncertainties are at 1σ c.l.. BMJD stands for Barycentric Modified Julian Date.

Epoch (BMJD)	Q_{opt}	U_{opt}	P_{opt} (%)	PA_{opt} ($^\circ$)
60465.9887	0.0131 ± 0.0014	-0.0009 ± 0.0014	1.43 ± 0.13	2.0 ± 2.8
60465.9915	0.0127 ± 0.0014	0.0009 ± 0.0014	1.44 ± 0.13	-0.1 ± 2.7
60465.9943	0.0101 ± 0.0014	0.0005 ± 0.0014	1.01 ± 0.13	2.8 ± 3.8
60465.9971	0.0074 ± 0.0014	-0.0037 ± 0.0014	0.97 ± 0.13	-7.6 ± 4.0
60465.9999	0.0129 ± 0.0014	-0.0012 ± 0.0014	1.51 ± 0.14	-2.4 ± 2.6
60466.0027	0.0090 ± 0.0014	-0.0044 ± 0.0012	1.03 ± 0.13	-4.7 ± 3.2
60466.0055	0.0131 ± 0.0014	-0.0069 ± 0.0013	2.12 ± 0.13	-12.3 ± 1.9
60466.0083	0.0113 ± 0.0014	-0.0041 ± 0.0014	1.60 ± 0.13	-11.4 ± 2.1
60466.0112	0.0101 ± 0.0014	-0.0018 ± 0.0014	1.12 ± 0.14	-0.3 ± 3.5
60466.0140	0.0129 ± 0.0014	0.0021 ± 0.0014	1.57 ± 0.13	5.9 ± 2.5
60466.0168	0.0138 ± 0.0014	-0.0028 ± 0.0014	1.64 ± 0.14	-4.9 ± 2.4
60466.0196	0.0152 ± 0.0014	-0.0030 ± 0.0014	1.57 ± 0.14	0.3 ± 2.5
60466.0225	0.0108 ± 0.0014	0.0023 ± 0.0014	1.11 ± 0.14	-2.5 ± 3.5
60466.0253	0.0106 ± 0.0014	-0.0037 ± 0.0014	1.19 ± 0.13	-7.3 ± 3.3

During the low mode episode, we observe an increase in the optical emission by a factor of 1.3, which contrasts with the behavior seen in the X-ray and UV bands. The origin of this optical increase is unclear, but it may be related to the broadening or enhanced prominence of hydrogen $H\alpha$ and/or three helium He I emission lines. These lines, possibly originating from regions within the accretion disk or from mass outflows, fall within the wavelength range of the R filter of FORS2 (572.5–737.5 nm). A recent high-time-resolution optical spectroscopic study of J1023 using the OSIRIS spectrograph mounted on the *GranTeCan* reported significant variability in the equivalent width and full width at half maximum of these lines, such as changes by a factor of two over minute timescales for the $H\alpha$ line, with no clear correlation with the flux of the optical continuum [89] (see also [110, 59] for further evidence of highly variable emission line profiles). In contrast, no prominent emission lines are expected within the wavelength range of the UVM2 filter of the *Swift* UVOT, as shown in the UV spectrum by [63]. We emphasize that if the optical emission lines originate from an outflow, this observation would lend support to scenarios suggesting stronger outflows during the low mode [122, 10], which also result in increased radio emission. However, since similar variability in the optical light curve is also observed in other instances during the X-ray high mode, it is not possible to draw a definitive conclusion.

P_{opt} exhibits moderate time variability, with a Median Absolute Deviation (MAD) of 0.23% and a normalized Excess Variance (NEV) of 0.05, indicating some intrinsic fluctuations. Its skewness is 0.58, suggesting a slight right-skewed distribution and indicating that deviations above the mean are more frequent. On the other hand, PA_{opt} shows greater variability, with a MAD of 3.6° , a significantly higher NEV of 12.7, and a skewness of -0.23, pointing to a slight left-skewed distribution where de-

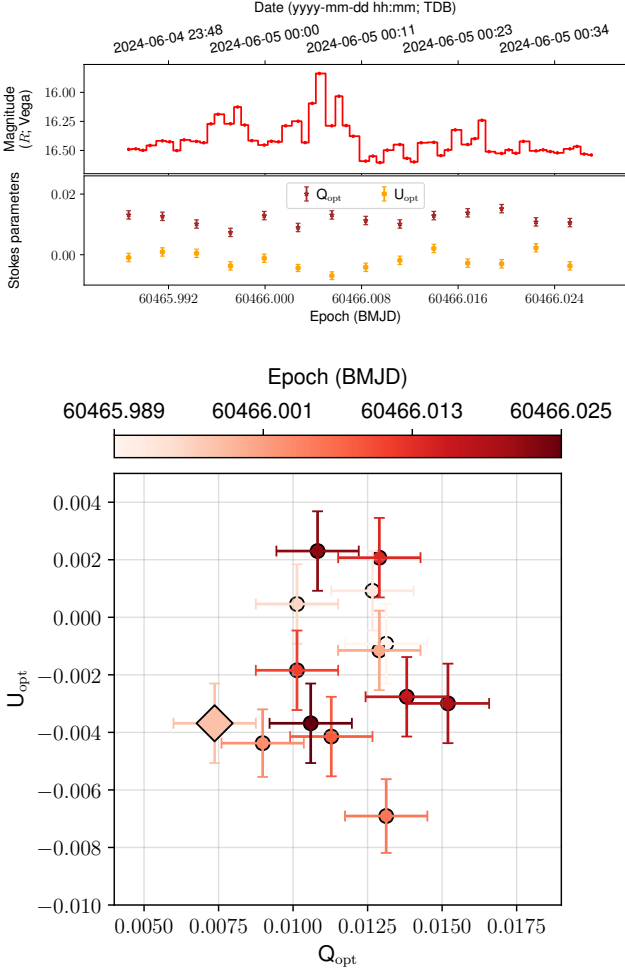


Figure 14: Top: time evolution of optical intensity (red) and of the Q_{opt} (brown) and U_{opt} (orange) Stokes parameters. Bottom: Scatter plot of Stokes parameters for the optical emission from J1023. Data points are color-coded based on the time of their measurements, with a diamond marker highlighting the epoch corresponding to the low mode detected during simultaneous X-ray observations. BMJD stands for Barycentric Modified Julian Date. TDB indicates the Barycentric Dynamical Time.

viations below the mean are more common. The opposite trends in the skewness of P_{opt} and PA_{opt} are primarily due to their anticorrelated variability during the second peak of optical intensity (Figures 1 and 14). We measure $P_{\text{opt,H}} = (1.41 \pm 0.04)\%$ and $PA_{\text{opt,H}} = -3.9^\circ \pm 0.7^\circ$ for the high mode; $P_{\text{opt,L}} = (0.97 \pm 0.13)\%$ and $PA_{\text{opt,L}} = -7.6^\circ \pm 4.0^\circ$ for the low mode. Consistent with previous findings by [10], these measurements suggest a slight decrease in polarization degree when switching from the high to the low mode, while the polarization angle shows no significant variation within the uncertainties.

Figure 14 shows the time series of the Q_{opt} and U_{opt} Stokes parameters. The two parameters exhibit distinct variability patterns. Q_{opt} exhibits relatively low variability, with a MAD of 0.0013 and a NEV of 0.03, indicating minimal intrinsic fluctuation. Its skewness is -0.33, suggesting a slightly left-skewed distribution with more frequent deviations below the mean. U_{opt} shows more pronounced variability, with a MAD of 0.0016 and a significantly higher NEV of 1.8, indicating substantial intrinsic fluctuations. The skewness is 0.04, indicating an almost symmetric distribution, with a very slight tendency for deviations above the mean. These results suggest that U_{opt} is more variable and less symmetric than Q_{opt} .

Figure 14 also shows the Q_{opt} and U_{opt} Stokes parameters of J1023 on the $Q_{\text{opt}} - U_{\text{opt}}$ plane for the whole dataset, including high modes (filled dots) and the low mode (filled diamond). The data points are color-coded according to the time they were recorded. Despite some intrinsic variation, the Q_{opt} and U_{opt} values cluster around a common point, and there is no clear distinction between the high and low modes.

F Polarization Properties in the Low Mode; Constraints on Polarized Radio Emission in the two Modes

In the scenario outlined in Section 4.1.4, the upper limit on the radio linear polarization fraction in the high mode is consistent with partially self-absorbed synchrotron radiation from the optically thick portion of the compact jet. The exact cause of the switch to the low mode remains uncertain, though the detection of short millimeter-band flares during a few of these switches in past observations points to sudden ejections of magnetized plasma, likely originating from the innermost regions of the accretion flow. The ejection of this matter could thus force the shock region to move outward, reducing the X-ray flux and the pulsed emission. As the plasma propagates downstream in the compact jet, it becomes op-

tically thin in the radio band [10]. This framework also accounts for the optical polarization properties measured during the low mode. If the shock moves outward, it may still contribute a measurable amount of polarized light. Moreover, the optical polarization angle observed in the low mode is consistent with that of the high mode within uncertainties, suggesting a common underlying emission mechanism for the optical linear polarization across both modes and reinforcing the idea that residual shock emission remains active in the low mode. In the soft X-ray band, where the jet could dominate up to 100% of the emission [10], the maximum expected polarization would be $\simeq 25\%$. The upper limit for the X-ray polarization degree during the low mode, $P_{X,L} < 26\%$ at a 90% c.l., makes it impossible to draw firm conclusions from this measurement. Alternatively, the switch to the low mode may result from matter occasionally penetrating the light cylinder, temporarily forcing the system into a regime where the rapidly rotating magnetic field anchored to the NS propels the inflowing matter away. As matter expands outward, it becomes increasingly rarefied and more transparent to synchrotron emission at radio wavelengths [122].

At radio wavelengths, synchrotron radiation is expected to produce linear polarization fractions of up to 10% for optically thick emission and up to 70% for optically thin emission, assuming uniform magnetic fields and a power-law electron distribution with an index of $\simeq 2$ [85]. In accreting stellar-mass black holes, polarization fractions are typically below 10%, but can reach up to 50% during instances of optically thin emission ([68] and references therein). Thus, the upper limit on the linear polarization measured from J1023 in the high mode is consistent with the presence of an optically thick compact jet, similar to what is observed in other X-ray binaries. In contrast, the lower polarization limit during the low mode may result from partial cancellation of orthogonally polarized jet components due to misaligned magnetic fields.

G Polarimetric properties of accreting neutron stars in LMXBs

IXPE has observed several accreting NSs in LMXBs, revealing diverse polarimetric behaviors. The polarization degree of the soft X-ray emission typically remains around a few percent across all observed systems. In this section, we summarize the polarization properties of the observed systems and briefly discuss their interpretations.

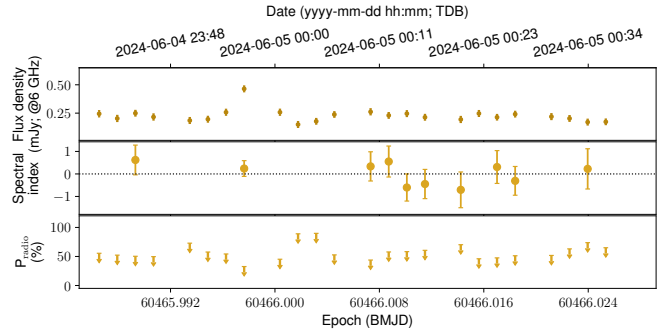


Figure 15: Evolution of the radio properties. The panels, from top to bottom, illustrate the temporal evolution of the radio flux density at the central frequency of 6 GHz in the VLA’s C-band; the spectral index, calculated by dividing the 4–8 GHz band into two sub-bands (4–6 GHz and 6–8 GHz); and the 3σ upper limits on the linear polarization fraction. Each time bin represents a 2-min interval. Spectral indices are only shown when they are constrained, with the horizontal dotted line marking a spectral index of 0 (i.e., a flat spectrum). BMJD stands for Barycentric Modified Julian Date, TDB for Barycentric Dynamical Time.

G.1 Z-sources

Cyg X–2. Cyg X-2 exhibits stable spectral characteristics along the Z-track, with a notable hard X-ray excess above 30 keV during the Horizontal Branch phase linked to episodic radio jet emissions. *IXPE* measurements indicate a polarization degree of $1.8\% \pm 0.3\%$ and a PA of $140^\circ \pm 4^\circ$, aligning with the radio jet direction. The Comptonized emission component shows a polarization degree of $4.0\% \pm 0.7\%$, also aligned with the jet, suggesting the primary polarization originates from a spreading layer on the NS surface, with potential contributions from disk reflection [48].

Sco X–1. Sco X–1 is the brightest persistent extra-solar X-ray source, approaching the Eddington luminosity for a $1.4 M_\odot$ NS. It has a 19-hour orbital period and it is located 2.13 kpc away. *IXPE* observations in the soft state revealed an average PD of $1.0\% \pm 0.2\%$ and a PA of $8^\circ \pm 6^\circ$. The PD of the accretion disk emission was constrained to $< 3.2\%$, while that of the Comptonized component was $1.3\% \pm 0.4\%$ [78].

GX 5–1. GX 5–1 is located near the Galactic Center and is notable for radio emission from a compact jet. *IXPE* observations in the horizontal and normal-flaring branches of the Z-track measured PDs of $3.7\% \pm 0.4\%$ and $1.8\% \pm 0.4\%$, respectively. A $\simeq 20^\circ$ variation in PA with energy was observed, likely due to differing polarization angles of the disk and Comp-

tonization components peaking at various energies [46].

GX 340+0. GX 340+0 is known for its stable spectral behavior and associated radio jet emissions. *IXPE* observations detected significant X-ray polarization when the source was mainly within the horizontal branch, with a PD of $4.0\% \pm 0.4\%$ and a PA of $38^\circ \pm 3^\circ$ in the 2–8 keV range. A variation in polarization angle with energy was measured, which was attributed to either the accretion disk and Comptonized emissions, or a mix of blackbody emission and Comptonized emission [13]. Alternatively, the low-energy polarization could be due to the accretion disk whereas the high energy polarization could arise from the corona [79]. Subsequent observations during the normal branch phase recorded a PD of $1.2\% \pm 0.3\%$ and a PA of $38^\circ \pm 6^\circ$, with the PD exhibiting a marginal increase with energy. The PA is consistent with that measured in the horizontal branch. The observed polarized emission is consistent with originating from blackbody emission, Comptonized emission, or reflection features, with no significant contribution from the accretion disk [13].

G.2 Atoll sources

GS 1826–238. GS 1826–238 remained in a hard spectral state until its transition to a high soft state in early 2016. *IXPE* observations in 2022 set a 3σ upper limit on the PD of 1.3% [25].

GX 3+1 GX 3+1 was observed with *IXPE*, along with *NuSTAR* and *NICER*, in August 2024. No significant X-ray polarization was detected in the 2–8 keV band, with an upper limit of 1.3% on the PD at the 99% c.l. The X-ray spectra are well described by a model consisting of thermal emission from an accretion disk, a Comptonized emission component, and a component accounting for reflected photons off the disk. The upper limits on the polarized signal from the disk and the Comptonization component are consistent with theoretical expectations for a system with a standard disk and a Comptonizing region that likely has a geometry consistent with a spreading layer [53].

GX 9+9. GX 9+9 exhibits a consistent bright soft state and a 4.2-hour modulation in both optical and X-ray bands. A spectro-polarimetric analysis of *IXPE* data detected X-ray polarization with a PD of $1.7\% \pm 0.4\%$ in the 2–8 keV band, which increased from a value consistent with null polarization in the 2–4 keV range to 3.2% in the 4–8 keV range. Spectral modeling indicated that the emission comprises thermal radiation from the accretion disk and a Comptonized component from an optically thick corona, suggesting that the polarization primarily originates from the Comptonized component [29]. A subsequent

study measured a PD of $2.2\% \pm 0.5\%$ in the 4–8 keV band. Broadband spectral modeling required thermal disk emission, a Comptonized component, and a reflection component. An upper limit of 4% was found on the PD of the disk emission; both Comptonization near the NS and disk reflection were found to contribute to the observed polarization [118].

4U 1624–49. 4U 1624–49 is a persistent system known for its periodic 6–8 hour dips every 21 hours and flaring behavior above the bright persistent emission. *IXPE* detected an average PD of $3.1\% \pm 0.7\%$ and a PA of $81^\circ \pm 6^\circ$ during non-dip intervals, with PD increasing from $3.0\% \pm 0.9\%$ (4–6 keV) to $6\% \pm 2\%$ (6–8 keV). This suggests polarization arises from Comptonization in an extended, geometrically thin slab corona covering part of the accretion disk and disk reflection. During X-ray dips, an upper limit of 22% was established for the PD [108, 54].

G.3 Ultracompact binaries

4U 1626–67. 4U 1626–67 is a 7.66-s pulsar in an ultracompact binary with a 42-minute orbital period. *IXPE* observations constrained the pulse-averaged PD to $<4\%$ (95% confidence). However, phase-resolved spectro-polarimetric analysis revealed a marginal polarization detection in the power-law component with a PD of $4.8\% \pm 2.3\%$ (90% confidence; [88]).

4U 1820–303. 4U 1820–303 is an ultra-compact low-mass X-ray binary located in the globular cluster NGC 6624 at ≈ 8 kpc. The system features a 11-minute orbital period and exhibits luminosity variations over a 170-day super-orbital cycle. Its spectrum comprises a blackbody or multicolor disk component, a Comptonization component, and an iron $K\alpha$ line around 6.5 keV. *IXPE* observations measured a PD of $2.0\% \pm 0.5\%$ with a PA of $-55^\circ \pm 7^\circ$ in the 4–7 keV band and $10\% \pm 2\%$ with a PA of $-67^\circ \pm 7^\circ$ in the 7–8 keV band. spectro-polarimetric analysis suggests orthogonal polarization between the accretion disk and the hard spectral component from the boundary/spreading layer [40].

G.4 Transient systems

XTE J1701–462. This transient system experienced an outburst in September 2022, and was observed twice by *IXPE* with a 10-day interval. The initial observation was performed when the source was in the horizontal branch and recorded an average PD of $4.5\% \pm 0.4\%$, increasing from $3.9\% \pm 0.3\%$ (2–4 keV) to $5.5\% \pm 0.6\%$ (4–8 keV). The subsequent observation, taken in the normal branch, showed a reduced average PD of $\simeq 0.6\%$. Spectral modeling incorporated an unpolarized

thermal emission from the accretion disk and a Comptonized component with a PD of $7.7\% \pm 2.5\%$, indicating the Comptonized emission likely originates from a spreading or boundary layer above the NS surface, decreasing at later outburst stages [32, 72, 133]. A recent time-resolved polarimetric analysis revealed a stable PD of $\simeq 2\%$ in the second observation along with significant variations in the PA (yielding depolarization in the time-averaged data and hence the smaller average PD). These results point to rapid changes in the geometry of the corona, possibly from a slab geometry to a more vertically extended spreading layer geometry [134].

SRGA J144459.2–604207.

SRGA J144459.2–604207 is an accreting MSP detected in outburst in February 2024. Over a 10-day monitoring period, *IXPE* measured an average PD of $2.3\% \pm 0.4\%$ in the 2–8 keV band, with a PA of $59^\circ \pm 6^\circ$. The polarization exhibited significant energy dependence, reaching $4.0\% \pm 0.5\%$ between 3 and 6 keV, while remaining below 2% (90% c.l.) in the 2–3 keV range. No significant variability in the polarization properties was detected across spin and orbital phases. The observations are consistent with a moderately fan-beam emission originating from two localized hotspots with a small magnetic obliquity of $\approx 10^\circ$. An upper limit on the PD of 8.5% (90% c.l.) was set during type I bursts [99].

G.5 Other systems

GX 13+1. GX 13+1 is a bright, persistent Galactic type I X-ray burster. *IXPE* observations in October 2023 detected a PD of $1.4\% \pm 0.3\%$ (2–8 keV) with a PA of $-2^\circ \pm 6^\circ$. A follow-up observation in February 2024 measured an overall PD of 2.5% and a PA of 24° . The polarization was attributed to a combination of Comptonization in the boundary or spreading layer and scattering from the accretion disk wind [17, 15].

References

- [1] Alpar, M. A., Cheng, A. F., Ruderman, M. A., & Shaham, J. 1982, *Nature*, 300, 728, doi: 10.1038/300728a0
- [2] Appenzeller, I., Fricke, K., Fürtig, W., et al. 1998, *The Messenger*, 94, 1
- [3] Archibald, A. M., Kaspi, V. M., Hessels, J. W. T., et al. 2013, arXiv e-prints, arXiv:1311.5161. <https://arxiv.org/abs/1311.5161>
- [4] Archibald, A. M., Stairs, I. H., Ransom, S. M., et al. 2009, *Science*, 324, 1411, doi: 10.1126/science.1172740
- [5] Archibald, A. M., Bogdanov, S., Patruno, A., et al. 2015, *ApJ*, 807, 62, doi: 10.1088/0004-637X/807/1/62
- [6] Arnaud, K. A. 1996, in *Astronomical Data Analysis Software and Systems V*, Vol. 101, XSPEC: The First Ten Years, ed. G. H. Jacoby & J. Barnes (ASP, San Francisco), 17–20
- [7] Astropy Collaboration, Price-Whelan, A. M., Lim, P. L., et al. 2022, *ApJ*, 935, 167, doi: 10.3847/1538-4357/ac7c74
- [8] Baglio, M. C., D’Avanzo, P., Campana, S., et al. 2016, *A&A*, 591, A101, doi: 10.1051/0004-6361/201628383
- [9] Baglio, M. C., Russell, D. M., Crespi, S., et al. 2020, *ApJ*, 905, 87, doi: 10.3847/1538-4357/abc685
- [10] Baglio, M. C., Coti Zelati, F., Campana, S., et al. 2023, *A&A*, 677, A30, doi: 10.1051/0004-6361/202346418
- [11] Baldini, L., Bucciantini, N., Di Lalla, N., et al. 2022, *SoftwareX*, 19, 101194, doi: 10.1016/j.softx.2022.101194
- [12] Baldini, L., Barbanera, M., Bellazzini, R., et al. 2021, *Astroparticle Physics*, 133, 102628, doi: 10.1016/j.astropartphys.2021.102628
- [13] Bhargava, Y., Ng, M., Zhang, L., et al. 2024, arXiv e-prints, arXiv:2405.19324, doi: 10.48550/arXiv.2405.19324
- [14] Bobrikova, A., Di Marco, A., La Monaca, F., et al. 2024, *A&A*, 688, A217, doi: 10.1051/0004-6361/202450207
- [15] —. 2024, *A&A*, 688, A217, doi: 10.1051/0004-6361/202450207
- [16] Bobrikova, A., Loktev, V., Salmi, T., & Poutanen, J. 2023, *A&A*, 678, A99, doi: 10.1051/0004-6361/202346833
- [17] Bobrikova, A., Forsblom, S. V., Di Marco, A., et al. 2024, *A&A*, 688, A170, doi: 10.1051/0004-6361/202449318
- [18] Bogdanov, S., Archibald, A. M., Bassa, C., et al. 2015, *ApJ*, 806, 148, doi: 10.1088/0004-637X/806/2/148
- [19] Bogdanov, S., Deller, A. T., Miller-Jones, J. C. A., et al. 2018, *ApJ*, 856, 54, doi: 10.3847/1538-4357/aaaeb9

- [20] Bucciattini, N., Ferrazzoli, R., Bachetti, M., et al. 2023, *Nature Astronomy*, 7, 602, doi: 10.1038/s41550-023-01936-8
- [21] Burrows, D. N., Hill, J. E., Nousek, J. A., et al. 2005, *Space Science Reviews*, 120, 165
- [22] Burtovoi, A., Zampieri, L., Fiori, M., et al. 2020, *MNRAS*, 498, L98, doi: 10.1093/mnrasl/slaa133
- [23] Campana, S., & Di Salvo, T. 2018, in *Astrophysics and Space Science Library*, Vol. 457, *Astrophysics and Space Science Library*, ed. L. Rezzolla, P. Pizzochero, D. I. Jones, N. Rea, & I. Vidaña, 149, doi: 10.1007/978-3-319-97616-7_4
- [24] Campana, S., Miraval Zanon, A., Coti Zelati, F., et al. 2019, *A&A*, 629, L8, doi: 10.1051/0004-6361/201936312
- [25] Capitanio, F., Fabiani, S., Gnarini, A., et al. 2023, *ApJ*, 943, 129, doi: 10.3847/1538-4357/acae88
- [26] CASA Team, Bean, B., Bhatnagar, S., et al. 2022, *PASP*, 134, 114501, doi: 10.1088/1538-3873/ac9642
- [27] —. 2022, *PASP*, 134, 114501, doi: 10.1088/1538-3873/ac9642
- [28] Cerutti, B., Mortier, J., & Philippov, A. A. 2016, *MNRAS*, 463, L89, doi: 10.1093/mnrasl/slw162
- [29] Chatterjee, R., Agrawal, V. K., Jayasurya, K. M., & Katoch, T. 2023, *MNRAS*, 521, L74, doi: 10.1093/mnrasl/slad026
- [30] Cheng, K. S., Ho, C., & Ruderman, M. 1986, *ApJ*, 300, 500, doi: 10.1086/163829
- [31] Cheng, K. S., Ruderman, M., & Zhang, L. 2000, *ApJ*, 537, 964, doi: 10.1086/309051
- [32] Cocchi, M., Gnarini, A., Fabiani, S., et al. 2023, *A&A*, 674, L10, doi: 10.1051/0004-6361/202346275
- [33] Coti Zelati, F., Campana, S., Braitto, V., et al. 2018, *A&A*, 611, A14, doi: 10.1051/0004-6361/201732244
- [34] Covino, S., Lazzati, D., Ghisellini, G., et al. 1999, *A&A*, 348, L1
- [35] Declair, M., Gordon, K. D., Andrews, J. E., et al. 2022, *ApJ*, 930, 15, doi: 10.3847/1538-4357/ac5dbe
- [36] Deller, A. T., Archibald, A. M., Brisken, W. F., et al. 2012, *ApJL*, 756, L25, doi: 10.1088/2041-8205/756/2/L25
- [37] Deller, A. T., Moldon, J., Miller-Jones, J. C. A., et al. 2015, *ApJ*, 809, 13, doi: 10.1088/0004-637X/809/1/13
- [38] Di Marco, A., Costa, E., Muleri, F., et al. 2022, *AJ*, 163, 170, doi: 10.3847/1538-3881/ac51c9
- [39] Di Marco, A., Fabiani, S., La Monaca, F., et al. 2022, *AJ*, 164, 103, doi: 10.3847/1538-3881/ac7719
- [40] Di Marco, A., Soffitta, P., Costa, E., et al. 2023, *AJ*, 165, 143, doi: 10.3847/1538-3881/acba0f
- [41] di Serego Alighieri, S. 1998, Cambridge University Press, 199, 287
- [42] Díaz Trigo, M., & Boirin, L. 2016, *Astronomische Nachrichten*, 337, 368, doi: 10.1002/asna.201612315
- [43] Dyks, J., Harding, A. K., & Rudak, B. 2004, *ApJ*, 606, 1125, doi: 10.1086/383121
- [44] Dyks, J., & Rudak, B. 2003, *ApJ*, 598, 1201, doi: 10.1086/379052
- [45] Elsner, R. F., O’Dell, S. L., & Weisskopf, M. C. 2012, in *Society of Photo-Optical Instrumentation Engineers (SPIE) Conference Series*, Vol. 8443, *Space Telescopes and Instrumentation 2012: Ultraviolet to Gamma Ray*, ed. T. Takahashi, S. S. Murray, & J.-W. A. den Herder, 84434N, doi: 10.1117/12.924889
- [46] Fabiani, S., Capitanio, F., Iaria, R., et al. 2024, *A&A*, 684, A137, doi: 10.1051/0004-6361/202347374
- [47] Farinelli, R., Waghmare, A., Ducci, L., & Santangelo, A. 2024, *A&A*, 684, A62, doi: 10.1051/0004-6361/202348915
- [48] Farinelli, R., Fabiani, S., Poutanen, J., et al. 2023, *MNRAS*, 519, 3681, doi: 10.1093/mnras/stac3726
- [49] Fitzpatrick, E. L., Massa, D., Gordon, K. D., Bohlin, R., & Clayton, G. C. 2019, *ApJ*, 886, 108, doi: 10.3847/1538-4357/ab4c3a
- [50] Foight, D. R., Güver, T., Özel, F., & Slane, P. O. 2016, *ApJ*, 826, 66, doi: 10.3847/0004-637X/826/1/66
- [51] Gehrels, N., Chincarini, G., Giommi, P., et al. 2004, *ApJ*, 611, 1005

- [52] Gendreau, K. C., Arzoumanian, Z., & Okajima, T. 2012, in *Society of Photo-Optical Instrumentation Engineers (SPIE) Conference Series*, Vol. 8443, *Space Telescopes and Instrumentation 2012: Ultraviolet to Gamma Ray*, ed. T. Takahashi, S. S. Murray, & J.-W. A. den Herder, 844313, doi: 10.1117/12.926396
- [53] Gnarini, A., Farinelli, R., Ursini, F., et al. 2024, *A&A*, 692, A123, doi: 10.1051/0004-6361/202452642
- [54] Gnarini, A., Lynne Saade, M., Ursini, F., et al. 2024, *A&A*, 690, A230, doi: 10.1051/0004-6361/202450716
- [55] Gordon, C., & Arnaud, K. 2021, *PyXspec: Python interface to XSPEC spectral-fitting program*, *Astrophysics Source Code Library*, record ascl:2101.014
- [56] Gordon, K. 2024, *The Journal of Open Source Software*, 9, 7023, doi: 10.21105/joss.07023
- [57] Gordon, K. D., Cartledge, S., & Clayton, G. C. 2009, *ApJ*, 705, 1320, doi: 10.1088/0004-637X/705/2/1320
- [58] Gordon, K. D., Clayton, G. C., Declair, M., et al. 2023, *ApJ*, 950, 86, doi: 10.3847/1538-4357/accb59
- [59] Hakala, P., & Kajava, J. J. E. 2018, *MNRAS*, 474, 3297, doi: 10.1093/mnras/stx2922
- [60] Harding, A. K. 2019, in *Astrophysics and Space Science Library*, Vol. 460, *Astronomical Polarisation from the Infrared to Gamma Rays*, ed. R. Mignani, A. Shearer, A. Słowikowska, & S. Zane, 277, doi: 10.1007/978-3-030-19715-5_11
- [61] Harding, A. K., & Muslimov, A. G. 2001, *ApJ*, 556, 987, doi: 10.1086/321589
- [62] Harris, C. R., Millman, K. J., van der Walt, S. J., et al. 2020, *Nature*, 585, 357, doi: 10.1038/s41586-020-2649-2
- [63] Hernandez Santisteban, J. V. 2016, PhD thesis, University of Southampton, UK
- [64] Hester, J. J., Mori, K., Burrows, D., et al. 2002, *ApJL*, 577, L49, doi: 10.1086/344132
- [65] Hobbs, G. B., Edwards, R. T., & Manchester, R. N. 2006, *MNRAS*, 369, 655
- [66] Högbom, J. A. 1974, *ApJS*, 15, 417
- [67] Hogg, D. W., & Foreman-Mackey, D. 2018, *ApJS*, 236, 11, doi: 10.3847/1538-4365/aab76e
- [68] Hughes, A. K., Sivakoff, G. R., Macpherson, C. E., et al. 2023, *MNRAS*, 521, 185, doi: 10.1093/mnras/stad396
- [69] Hunter, J. D. 2007, *Computing in Science & Engineering*, 9, 90, doi: 10.1109/MCSE.2007.55
- [70] Illiano, G., Papitto, A., Ambrosino, F., et al. 2023, *A&A*, 669, A26, doi: 10.1051/0004-6361/202244637
- [71] Jaodand, A., Archibald, A. M., Hessels, J. W. T., et al. 2016, *ApJ*, 830, 122, doi: 10.3847/0004-637X/830/2/122
- [72] Jayasurya, K. M., Agrawal, V. K., & Chatterjee, R. 2023, *MNRAS*, 525, 4657, doi: 10.1093/mnras/stad2601
- [73] Joye, W. A., & Mandel, E. 2003, in *Astronomical Society of the Pacific Conference Series*, Vol. 295, *Astronomical Data Analysis Software and Systems XII*, ed. H. E. Payne, R. I. Jedrzejewski, & R. N. Hook, 489
- [74] Kennedy, M. R., Clark, C. J., Voisin, G., & Breton, R. P. 2018, *MNRAS*, 477, 1120, doi: 10.1093/mnras/sty731
- [75] Kenyon, J. S., Perkins, S., & Smirnov, O. 2022, in *Astronomical Society of the Pacific Conference Series*, Vol. 532, *Astronomical Data Analysis Software and Systems XXX*, ed. J. E. Ruiz, F. Pierfederici, & P. Teuben, 349
- [76] Kislak, F., Clark, B., Beilicke, M., & Krawczynski, H. 2015, *Astroparticle Physics*, 68, 45, doi: 10.1016/j.astropartphys.2015.02.007
- [77] Krawczynski, H., Muleri, F., Dovčiak, M., et al. 2022, *Science*, 378, 650, doi: 10.1126/science.add5399
- [78] La Monaca, F., Di Marco, A., Poutanen, J., et al. 2024, *ApJL*, 960, L11, doi: 10.3847/2041-8213/ad132d
- [79] La Monaca, Fabio, Di Marco, Alessandro, Ludlam, Renee M., et al. 2024, *A&A*, 691, A253, doi: 10.1051/0004-6361/202451966
- [80] Leahy, D. A. 1987, *A&A*, 180, 275
- [81] Linares, M. 2014, *ApJ*, 795, 72, doi: 10.1088/0004-637X/795/1/72
- [82] Linares, M., De Marco, B., Wijnands, R., & van der Klis, M. 2022, *MNRAS*, 512, 5269, doi: 10.1093/mnras/stac720

- [83] Linares, M., Bahramian, A., Heinke, C., et al. 2014, *MNRAS*, 438, 251, doi: 10.1093/mnras/stt2167
- [84] Liu, K., Xie, F., Liu, Y.-h., et al. 2023, *ApJL*, 959, L2, doi: 10.3847/2041-8213/ad0bfc
- [85] Longair, M. S. 2011, *High Energy Astrophysics* (Cambridge, UK: Cambridge University Press)
- [86] Luo, J., Ransom, S., Demorest, P., et al. 2021, *ApJ*, 911, 45, doi: 10.3847/1538-4357/abe62f
- [87] Lyutikov, M., Pariev, V. I., & Gabuzda, D. C. 2005, *MNRAS*, 360, 869, doi: 10.1111/j.1365-2966.2005.08954.x
- [88] Marshall, H. L., Ng, M., Rogantini, D., et al. 2022, *ApJ*, 940, 70, doi: 10.3847/1538-4357/ac98c2
- [89] Messa, M. M., D’Avanzo, P., Coti Zelati, F., Baglio, M. C., & Campana, S. 2024, *A&A*, 690, A344, doi: 10.1051/0004-6361/202449466
- [90] Miraval Zanon, A., Ambrosino, F., Coti Zelati, F., et al. 2022, *A&A*, 660, A63, doi: 10.1051/0004-6361/202243180
- [91] Monet, D. G., Levine, S. E., Canzian, B., et al. 2003, *AJ*, 125, 984
- [92] Nasa High Energy Astrophysics Science Archive Research Center (Heasarc). 2014, HEASoft: Unified Release of FTOOLS and XANADU. <http://ascl.net/1408.004>
- [93] Nitindala, A. P., Veledina, A., & Poutanen, J. 2024, arXiv e-prints, arXiv:2411.18299, doi: 10.48550/arXiv.2411.18299
- [94] Offringa, A. R., McKiconley, B., Hurley-Walker, N., et al. 2014, *MNRAS*, 444, 606, doi: 10.1093/mnras/stu1368
- [95] Papitto, A., & de Martino, D. 2022, in *Astrophysics and Space Science Library*, Vol. 465, *Astrophysics and Space Science Library*, ed. S. Bhattacharyya, A. Papitto, & D. Bhattacharyya, 157–200, doi: 10.1007/978-3-030-85198-9_6
- [96] Papitto, A., Ferrigno, C., Bozzo, E., et al. 2013, *Nature*, 501, 517, doi: 10.1038/nature12470
- [97] Papitto, A., Rea, N., Coti Zelati, F., et al. 2018, *ApJL*, 858, L12, doi: 10.3847/2041-8213/aabee9
- [98] Papitto, A., Ambrosino, F., Stella, L., et al. 2019, *ApJ*, 882, 104, doi: 10.3847/1538-4357/ab2fdf
- [99] Papitto, A., Di Marco, A., Poutanen, J., et al. 2024, arXiv e-prints, arXiv:2408.00608, doi: 10.48550/arXiv.2408.00608
- [100] Park, R. S., Folkner, W. M., Williams, J. G., & Boggs, D. H. 2021, *AJ*, 161, 105, doi: 10.3847/1538-3881/abd414
- [101] Patruno, A., Archibald, A. M., Hessels, J. W. T., et al. 2014, *ApJL*, 781, L3, doi: 10.1088/2041-8205/781/1/L3
- [102] Perez, F., & Granger, B. E. 2007, *Computing in Science and Engg.*, 9, 21–29, doi: 10.1109/MCSE.2007.53
- [103] Petre, R., Hwang, U., Holt, S. S., Safi-Harb, S., & Williams, R. M. 2007, *ApJ*, 662, 988, doi: 10.1086/518019
- [104] Pétri, J., & Kirk, J. G. 2005, *ApJL*, 627, L37, doi: 10.1086/431973
- [105] Reynolds, S. P., Gaensler, B. M., & Bocchino, F. 2012, *SSR*, 166, 231, doi: 10.1007/s11214-011-9775-y
- [106] Roming, P. W. A., Kennedy, T. E., Mason, K. O., et al. 2005, *Space Science Reviews*, 120, 95, doi: 10.1007/s11214-005-5095-4
- [107] Rybicki, G. B., & Lightman, A. P. 1979, *Radiative processes in astrophysics*
- [108] Saade, M. L., Kaaret, P., Gnarini, A., et al. 2024, *ApJ*, 963, 133, doi: 10.3847/1538-4357/ad235a
- [109] Shahbaz, T., Dallilar, Y., Garner, A., et al. 2018, *MNRAS*, 477, 566, doi: 10.1093/mnras/sty562
- [110] Shahbaz, T., Linares, M., Rodríguez-Gil, P., & Casares, J. 2019, *MNRAS*, 488, 198, doi: 10.1093/mnras/stz1652
- [111] Soffitta, P., Baldini, L., Bellazzini, R., et al. 2021, *AJ*, 162, 208, doi: 10.3847/1538-3881/ac19b0
- [112] Stappers, B. W., Archibald, A. M., Hessels, J. W. T., et al. 2014, *ApJ*, 790, 39, doi: 10.1088/0004-637X/790/1/39
- [113] Stella, L., & Angelini, L. 1992, in *Astronomical Society of the Pacific Conference Series*, Vol. 25, *Astronomical Data Analysis Software and Systems I*, ed. D. M. Worrall, C. Biemesderfer, & J. Barnes, 103

- [114] Stetson, P. B. 1987, *PASP*, 99, 191, doi: 10.1086/131977
- [115] Stringer, J. G., Breton, R. P., Clark, C. J., et al. 2021, *MNRAS*, 507, 2174, doi: 10.1093/mnras/stab2167
- [116] Strohmayer, T. E. 2017, *ApJ*, 838, 72, doi: 10.3847/1538-4357/aa643d
- [117] Takata, J., Chang, H. K., & Shibata, S. 2008, *MNRAS*, 386, 748, doi: 10.1111/j.1365-2966.2008.12877.x
- [118] Ursini, F., Farinelli, R., Gnarini, A., et al. 2023, *A&A*, 676, A20, doi: 10.1051/0004-6361/202346541
- [119] Ursini, F., Gnarini, A., Capitanio, F., et al. 2024, *Galaxies*, 12, 43
- [120] Vaillancourt, J. E. 2006, *PASP*, 118, 1340, doi: 10.1086/507472
- [121] Vaughan, S., Edelson, R., Warwick, R. S., & Uttley, P. 2003, *MNRAS*, 345, 1271, doi: 10.1046/j.1365-2966.2003.07042.x
- [122] Veledina, A., Nättilä, J., & Beloborodov, A. M. 2019, *ApJ*, 884, 144, doi: 10.3847/1538-4357/ab44c6
- [123] Veledina, A., & Pélicier, M. 2024, arXiv e-prints, arXiv:2412.08359. <https://arxiv.org/abs/2412.08359>
- [124] Verner, D. A., Ferland, G. J., Korista, K. T., & Yakovlev, D. G. 1996, *ApJ*, 465, 487
- [125] Virtanen, P., Gommers, R., Oliphant, T. E., et al. 2020, *Nat. Methods*, 17, 261, doi: 10.1038/s41592-019-0686-2
- [126] Weisskopf, M. C., Elsner, R. F., & O'Dell, S. L. 2010, in *Society of Photo-Optical Instrumentation Engineers (SPIE) Conference Series*, Vol. 7732, *Space Telescopes and Instrumentation 2010: Ultraviolet to Gamma Ray*, ed. M. Arnaud, S. S. Murray, & T. Takahashi, 77320E, doi: 10.1117/12.857357
- [127] Weisskopf, M. C., Soffitta, P., Baldini, L., et al. 2022, *JATIS*, 8, 026002, doi: 10.1117/1.JATIS.8.2.026002
- [128] Wes McKinney. 2010, in *Proceedings of the 9th Python in Science Conference*, ed. Stéfan van der Walt & Jarrod Millman, 56 – 61, doi: 10.25080/Majora-92bf1922-00a
- [129] Wijnands, R., Degenaar, N., Armas Padilla, M., et al. 2015, *MNRAS*, 454, 1371, doi: 10.1093/mnras/stv1974
- [130] Wilms, J., Allen, A., & McCray, R. 2000, *ApJ*, 542, 914
- [131] Xie, F., Di Marco, A., La Monaca, F., et al. 2022, *Nature*, 612, 658, doi: 10.1038/s41586-022-05476-5
- [132] Xie, F., Wong, J., La Monaca, F., et al. 2024, *ApJ*, 962, 92, doi: 10.3847/1538-4357/ad17ba
- [133] Yu, W., Bu, Q., Doroshenko, V., et al. 2024, arXiv e-prints, arXiv:2401.02658, doi: 10.48550/arXiv.2401.02658
- [134] Zhao, Q., Li, H., Tao, L., & Feng, H. 2024, arXiv e-prints, arXiv:2411.11352. <https://arxiv.org/abs/2411.11352>